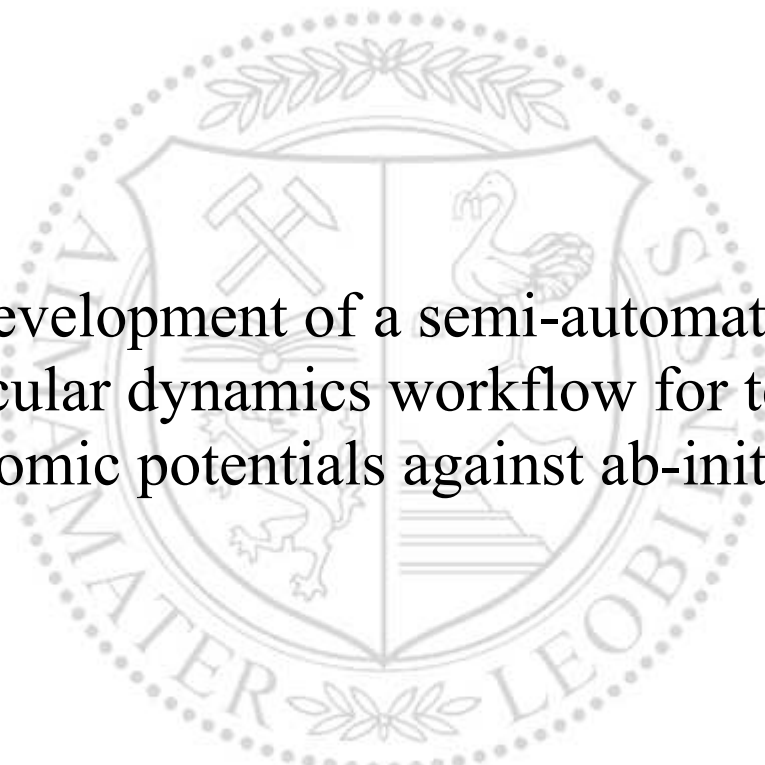Chair of Physical Metallurgy and Metallic Materials

Master's Thesis

Development of a semi-automated molecular dynamics workflow for testing interatomic potentials against ab-initio data

Celine Halkali, BSc

September 2022

EIDESSTATTLICHE ERKLÄRUNG

Ich erkläre an Eides statt, dass ich diese Arbeit selbständig verfasst, andere als die angegebenen Quellen und Hilfsmittel nicht benutzt, und mich auch sonst keiner unerlaubten Hilfsmittel bedient habe.

Ich erkläre, dass ich die Richtlinien des Senats der Montanuniversität Leoben zu "Gute wissenschaftliche Praxis" gelesen, verstanden und befolgt habe.

Weiters erkläre ich, dass die elektronische und gedruckte Version der eingereichten wissenschaftlichen Abschlussarbeit formal und inhaltlich identisch sind.

Datum 26.09.2022

Unterschrift Verfasser/in
Celine Halkali

Abstract

The experimental investigation of properties and behavior of materials has been increasingly complemented by computer-aided methods for several decades. Molecular dynamics simulations serve as a good combination of simple implementation and low computational effort with comparatively large system dimensions. Experiments on small scales tend to be cost-intensive and time-consuming. However, the knowledge of small scale processes in materials can give significant insight into bulk properties. This is also true for nickel-based superalloys, where e.g. the partitioning of species to various phases, grain boundaries and defects can lead to a considerable change in properties.

The aim of this work is to test interatomic potentials fitted to experimental data with respect to their comparability with results from ab-initio methods. Interatomic potentials developed for different, nickel-based material systems were tested for their applicability to face-centered cubic elemental nickel, body-centered cubic β-NiAl (B2), and face-centered cubic Ni$_3$Al (L1$_2$). Equilibrium lattice parameter, elastic properties, and nickel vacancy formation energy of all three phases, as well as the stacking fault, surface, and grain boundary energies of elemental nickel, were calculated and compared with results from ab-initio calculations.

Depending on the properties to which the potentials were fitted, the calculated values agree well with those obtained from ab-initio simulations. The results of the respective potentials for the equilibrium lattice parameters and elastic properties are in better agreement with the experimental values, since most of the time, they are parameters of the potential curves. The same is true for the vacancy formation energies if they were used for the potential development. Most of the stacking fault energies give satisfactory results. The surface energies, while generally lower than the ab-initio simulations, follow the $\gamma_{110} > \gamma_{100} > \gamma_{111}$ trend observed from these. Good results are obtained for the grain boundary energy, which was not included in the curve fitting for any of the potentials, but is still very close to the ab-initio results.

Most of the tested interatomic potentials are particularly suitable for the calculation of planar defect energies as a good part of these values agree well with those of the ab-initio calculations.

Kurzfassung

Die experimentelle Untersuchung von Eigenschaften und Verhalten von Werkstoffen wird bereits seit einigen Jahrzehnten zunehmend von computergestützten Methoden ergänzt. Hierbei zeichnen sich Molekulardynamik-Simulationen durch eine gute Kombination aus einfacher Implementierung und geringem Rechenaufwand bei vergleichsweise großen Systemabmessungen aus. Experimente in kleinem Maßstab sind in der Regel kostenintensiv und zeitaufwendig. Oft kann die Kenntnis von Vorgängen in kleinem Maßstab in Werkstoffen einen wichtigen Einblick in die Bulk-Eigenschaften geben. Dies ist auch bei Nickelbasis-Superlegierungen der Fall, deren Eigenschaften sich zum Beispiel durch Ausscheidung von Spezies in verschiedenen Phasen, an Korngrenzen oder anderen Kristallfehlern erheblich ändern können.

Ziel dieser Arbeit ist es, an experimentelle Daten angepasste interatomare Potentiale hinsichtlich ihrer Vergleichbarkeit mit Ergebnissen aus ab-initio-Methoden zu testen. Interatomare Potentiale, die für verschiedene, nickelbasierte Materialsysteme entwickelt wurden, wurden auf ihre Anwendbarkeit für kubisch-flächenzentriertes, elementares Nickel, kubisch-raumzentriertes β-NiAl (B2) und kubisch-flächenzentriertes Ni_3Al (L1$_2$) geprüft. Der Gleichgewichts-Gitterparameter, elastische Eigenschaften und die Leerstellenenergie aller drei Phasen, sowie die Stapelfehler-, Oberflächen- und Korngrenzenergien von elementarem Nickel wurden berechnet und mit Ergebnissen aus ab-initio-Berechnungen verglichen.

Abhängig von den Eigenschaften, an die die Potentiale angepasst wurden, stimmen die berechneten Werte gut mit denen der ab-initio-Simulationen überein. Die Ergebnisse der jeweiligen Potentiale für Gitterparameter und elastische Eigenschaften entsprechen eher den experimentellen Werten, da diese zumeist Parameter der Potentialkurven sind. Ähnliches gilt für die Nickel-Leerstellenenergien, wenn diese für die Potentialentwicklung verwendet wurden. Die meisten Stapelfehlerenergien führen zu zufriedenstellenden Ergebnissen. Die Oberflächenenergien fallen zwar generell niedriger als die ab-initio-Werte aus, folgen allerdings dem aus diesen bekannten Trend $\gamma_{110} > \gamma_{100} > \gamma_{111}$. Besonders hervorzuheben ist jedoch die Korngrenzenergie, die bei keinem der Potentiale in der Kurvenanpassung berücksichtigt wurde, den ab-initio-Ergebnissen aber sehr nahe kommt.

Die meisten der getesteten interatomaren Potentiale eignen sich vor allem für die Berechnung von Flächenfehlerenergien, da diese Werte mit denen der ab-initio-Berechnungen zum Teil sehr gut übereinstimmen.

Contents

List of Abbreviations

Abbreviation	Definition
bcc	Body-centered cubic
CA-PZ	Ceperley-Alder–Perdew-Zunger
DFT	Density functional theory
EAM	Embedded atom method
EAM/Alloy	Embedded atom method for alloys
EAM/FS	Embedded atom method –Finnis and Sinclair adaptation
fcc	Face-centered cubic
GGA	Generalized gradient approximation
HEA	High entropy alloy
LAMMPS	Large-scale atomic/molecular massively parallel simulator
LDA	Local density approximation
MC	Monte Carlo
MD	Molecular dynamics
MS	Molecular statics
MEAM	Modified embedded atom method
PBE	Perdew-Burke-Ernzerhof
PW86	Perdew-Wang 1986

List of Figures

List of Tables

1   Introduction

Complementing experiments by predicting material properties and processes with simulation methods has become a standard procedure in alloy development. Many different methods are available to choose from, depending on the desired phenomenon, size scale and accuracy, or material system. Density functional theory (DFT)-based methods pose an opportunity to calculate material properties with high accuracy. However, the computational effort for these calculations is quite high. The possibility of achieving DFT-level accuracy with faster methods is tempting. While molecular dynamics (MD) methods are often used to predict experimentally accessible properties, this thesis aims to evaluate the ability of MD simulations to imitate results from first-principles calculations.

The reliability of molecular dynamics simulations strongly depends on the interatomic potential used for a calculation. The embedded-atom method (EAM) provides a fast and simple way to develop such interatomic potentials. It has been subject of extensive research, and describes the properties of transition metals with nearly full or nearly empty d-bands very well [1]. Many interatomic potentials for nickel and its alloys have been developed as the properties of nickel-based material systems are relevant for high-temperature applications, e.g. the application of nickel-based superalloys in the aerospace industry. Intermetallic phases, such as the $\gamma\prime$ phase, play an important role in the high-temperature resistance of these alloys, and naturally, their properties have been studied extensively.

This thesis aims to verify the ability of different nickel-based, semi-empirical interatomic potentials to predict properties calculated with density function theory (DFT) methods. These potentials are almost exclusively fitted to experimental properties. However, the formalism of the EAM is based on the Hohenberg-Kohn theorem which is the foundation upon which density functional theory was developed [2]. As both simulation methods make use of this theorem, the capability of MD simulations with EAM potentials to calculate DFT properties is investigated. To conduct this study, a toolkit to compare material properties has been built on top of scripts that are freely available on the internet. The investigated potentials are based on the EAM, the modified embedded atom method (MEAM) and the Finnis and Sinclair variation of the EAM (EAM/FS).

2   Molecular dynamics

2.1   Differentiation from other atomistic methods

Molecular dynamics is one of the most common simulation methods in atomistic computational materials science, besides density functional theory (DFT) and Monte Carlo (MC). The most fundamental difference between all these methods is the smallest unit or element that the simulation system can be divided into. While DFT methods consider electrons and nuclei individually, the smallest unit considered in MD or MC methods is an atom. Electronic structure and hence bonding between atoms is calculated with quantum chemistry methods, during which the Schrödinger equation for the system is solved. The computational effort required to do so is extremely high, thus other electronic structure methods have emerged from it. While most of these methods use different approximations for the electronic wave function, density functional theory (DFT) assumes that a system of interacting electrons can be sufficiently described by a fictitious system of non-interacting particles. According to Hohenberg-Kohn's theorem [2], the energy of a system is a functional of its electronic density. The task that comes with this realization is to find a suitable expression for this electron density. The main problem is to find the exchange-correlation potential which is again a functional of the electronic density. There are multiple ways to approximate this term, one of the most common ones being the generalized gradient approximation (GGA) which takes into consideration that electron density is not constant throughout the whole crystal. This approximation has a tendency of underestimating the binding energies between atoms, and therefore overestimating lattice parameters. In contrast, the local density approximation (LDA) often overestimates binding energies, and often predicts materials to be stiffer than they really are [3, 4].

The size and complexity of systems for which DFT calculations can be carried out is very limited. While some material properties can be derived from electronic structure and bonding alone, the interatomic interaction between constituting atoms allows to simulate properties and phenomena which only occur on larger scales. The next larger scale is the atomistic scale. There are two major methods in which a single atom is the smallest unit that the simulation system can be divided into. While Monte Carlo simulations can predict rate-dependent phenomena such as diffusion very well, this approach is limited to problems of statistical/probabilistic nature. The second method is molecular dynamics. They are based on the simple idea to apply Newtonian/classical mechanics to atoms, i.e. treat them as particles. Apart from the initial conditions of the system, i.e. positions and velocities of the atoms, the most important input needed to solve the equation of motion for each atom are the forces or bonding energies between atoms in a system. The

entirety of these interatomic energies describes the bonding of a material as a function
– the interatomic potential. In the simplest form, it results from the potential energy
between two atoms as a function of their distances and it is used as an input value for
MD simulations. While these energies can be calculated very accurately with quantum
mechanical methods as described above, there are much faster approaches to approximate
these interactions. They can be determined semi-empirically by fitting the interatomic
potential curve to e.g. experimental or ab initio data, which will be explained in detail in
Section 2.3 [3, 4].

2.2 Fundamentals

Considering particle-based simulation techniques, two methods are mainly mentioned:
Monte Carlo simulations and molecular dynamics. However, molecular dynamics has
developed to be an umbrella term that also includes molecular statics calculations. Both
methods are based on the relation between the force acting upon an atom and its potential
energy:

$$F = -\nabla U = \frac{dU}{dr}. \tag{1}$$

In molecular dynamics, the trajectories of the atoms over time are evaluated by numeri-
cally integrating Newton's equation of motion

$$\frac{d^2r}{dt^2} = \frac{F}{m}, \tag{2}$$

from which dynamic material properties can be obtained. While molecular dynamics
simulation provide the time evolution of a system, molecular statics aims to find the
equilibrium configuration of atoms in the system. Material properties like the equilibrium
lattice parameter or the cohesive energy, i.e. the difference of the energy of a free atom and
of an atom in the bulk material, can be determined with molecular statics simulations. In
molecular statics, the goal is to find the minimum energy configuration of a system, i.e. the
positions of a systems constituting atoms at zero temperature. This is accomplished by
iteratively displacing the atoms along the direction of the acting forces until the potential
energy of the system is minimal. To determine this configuration, different methods,
such as the steepest descent method or the conjugate gradient method, can be applied.
Contrary to the displacement of atoms in MD simulations, these minimization processes
do not describe actual physical movement and cannot be used to make any statements
about the systems evolution over time. An interatomic potential curve provides the
energies based on which the minimum energy configuration of the system can be found.
These curves must be provided as input parameters, and can be determined with semi-
empirical or machine-learning methods. The quality of a MS or MD simulation is strongly

influenced by the choice of interatomic potentials, as they can be developed to describe only specific types of properties [3–5].

2.3 Interatomic potentials

Atomic bonding results from attractive and repulsive forces caused by the ionic cores and electrons of an element or material. Those forces and hence, the systems potential, change with interatomic distance. Functions aiming to describe interatomic bonding are called interatomic potentials. A schematic of an interatomic potential as a function of interatomic distance is shown in Figure 1. Some characteristic properties of a material or material system can be obtained directly from it. At 0 K, the interatomic distance at which the attractive and repulsive forces cancel each other out, and thus lead to the minimum energy configuration of the solid, is called equilibrium lattice parameter. The depth of the potential well at this distance is the cohesive energy.
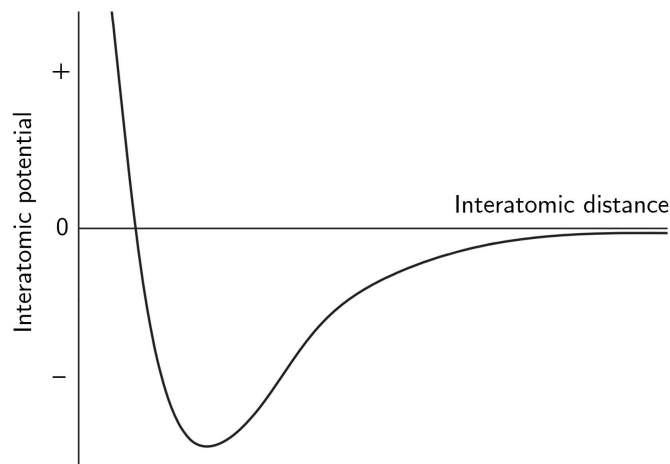
Figure 1: A schematic interatomic potential, adopted from [4].

While these interactions can be calculated via electronic structure methods, the calculations become considerably more complicated with increasing system sizes. A different approach to calculate properties of materials at these larger scales is needed. Molecular dynamics simulations cannot be used for electronic and magnetic properties because they do not consider nuclei and electrons separately, but numerous other properties can be calculated with this method. The input needed to perform these calculations are interatomic potentials, from which the forces acting on the different atoms can be obtained as described in Equation (1).

Depending on the bonding type, there are different approaches to describe these interatomic potentials. One of the simplest types of interatomic potentials is the Lennard-Jones potential, which is a pair potential. The repulsive term in it is based on electro-

static Coulomb interactions as well as the Pauli exclusion principle, while the attractive term arises from long-range van-der-Waals interactions. The Lennard-Jones potential is therefore suitable to model nobel gases. Modelling metallic materials, however, is more complex. The metallic bond is characterized by its positively charged nuclei and the core electrons with positions well approximated by the position of the corresponding nuclei and the electron cloud, in which (ideally speaking) all outer electrons are shared between all ionic cores within the solid. Although during the simulation the particles are treated without distinguishing between the nuclei and electrons, they are treated separately during potential development. In the following sections, one of the most common approaches to model metals, the embedded atom method, is presented.

2.3.1 The embedded atom method (EAM)

Due to the structure of the metallic bond, the interactions between nuclei and electrons are very different from those of noble gases. It cannot be described by a pair potential because the valence electrons are shared between all ionic cores and the bond does not depend solely on interactions between individual pairs of atoms. These interactions can only be considered in so-called many-body potentials.

A central problem arising with the use of pair potentials for metallic systems is that elastic properties cannot be calculated reliably. Metals can be deformed and are, to some extent, compressible. During these processes, the interactions between nuclei and electron cloud change. One way to include the energy contribution of the electron cloud, and hence a many-body interaction, was proposed by Johnson in [6] by adding a volume-dependent term. While this improves the possibility of calculating elastic properties, many material properties are not derived from changes in volume, but from changes in electron density. Not only do those material properties not depend on a volume change, they can also make it very difficult to define said volume. An alternative has been proposed by Daw and Baskes which has become one of the most common methods to develop interatomic potentials for metallic material systems: the embedded-atom method [7]. In the embedded-atom method, the problem of determining the volume of a system is bypassed by including an energy term that depends on the local electron density. The basic idea behind this approach is to treat every atom core, i.e. the ionic core and the inner electrons, as an impurity in the system of atoms making it up: It needs to be embedded in the background electron density provided by all the other atoms in the solid − hence the name. This embedding energy is a functional of the electron density [2], and is determined empirically in EAM potentials. To successfully describe metallic systems, a second, repulsive energy contribution originating from core-core interactions needs to be included in the total energy with a separate term. The general form of the total energy

consisting of those two components is as follows:

$$U = \sum_i F_i \left(\sum_{i \neq j} \rho_{h,i}(r_{ij}) \right) + \frac{1}{2} \sum_{i \neq j} \phi_{ij}(r_{ij}), \tag{3}$$

where the embedding energy F_i is a function of the electron density $\rho_{h,i}$ provided by the host in which the atom is embedded in, which itself is assumed to depend solely on atomic positions. The second term (ϕ_{ij}) is a doubly-screened pair potential to account for the electrostatic repulsion of the cores. Both electron density and pair potential are functions of the interatomic distance r_{ij}. The host electron density is simply a linear superposition of electronic densities of the neighboring atoms of the atom to be embedded:

$$\rho_{h,i}(r_{ij}) = \sum_j \rho_j(r_{ij}), \tag{4}$$

and each single atomic density ρ_j is based on density functional theory ideas. However, changes of the electronic configuration in alloys are not considered in the spherically averaged atomic densities calculated with the Hartree-Fock method. Therefore, Daw and Baskes introduced an expression for the "s-like content of the atomic densities" [7]:

$$\rho(r) = n_s \rho_s(r) + (N - n_s)\rho_d(r) = n_s \rho_s(r) + n_d \rho_d(r), \tag{5}$$

where n_s and n_d stand for the number of s- and d-electrons, ρ_n and ρ_d for the densities associated with the respective orbitals, and N for the total number of valence electrons.

The Coulombic pair potential used in the EAM is a assumed to be a simple geometric mean:

$$\phi_{ij}(r_{ij}) = \frac{Z_i(r_{ij}) Z_j(r_{ij})}{r_{ij}}. \tag{6}$$

Here, $Z(r)$ describes the effective charge. Its parametrized form as described in [8] is as follows:

$$Z(r) = Z_0(1 + \beta r^v)e^{\alpha r}, \tag{7}$$

where Z_0 is the same as N, the total number of valence electrons, and the three parameters α, β and ν have to be determined empirically.

While the embedding energy was fitted to material properties such as the lattice constant, cohesive energy and elastic constants in the original EAM, Foiles [9] adjusted this method for alloy systems, where the embedding energy does not change with the atomic species providing the background electron density. By fitting it to the Rose equation of state (EOS) [10]

$$E(a) = -E_{coh}(1 + a^*)e^{-a^*}, \tag{8}$$

the same concept could be applied to pure materials as well as alloys and has become the new standard for EAM potentials. In Equation 8, E_{coh} denotes the cohesive energy,

a the lattice constant, and the parameter a^* describes the deviation from the equilibrium lattice parameter as follows:

$$a^* = \sqrt{\frac{9B\Omega}{E_{coh}}} \left(\frac{a}{a_0} - 1\right) = \alpha \left(\frac{a}{a_0} - 1\right). \tag{9}$$

B stands for the bulk modulus, a_0 for the equilibrium lattice parameter, and Ω for the equilibrium atomic volume. For fcc metals, Ω is calculated as follows [11]:

$$\Omega = \frac{a^3}{4}. \tag{10}$$

As mentioned above, the electronic densities are described to be spherically averaged in the EAM. This assumption work well for fcc crystals with nearly full or nearly empty d-bands, where covalent and hence, directional bonding plays practically no role[1]. Two important adaptations of the EAM have emerged shortly after its initial derivation, and which wil be described briefly in the following to subsections.

2.3.2 Finnis and Sinclair potential (EAM/FS)

Directly after the embedded atom method had been developed, Finnis and Sinclair proposed another scheme to describe the interatomic potential curve of transition metals [12]. Their derivation allows to account for different bond strengths, and therefore consider the directionality of bonding in their method. While they base their method on the same idea as the EAM—they describe the energy of a metallic systems as the sum of a many-body interaction term and a simple pair potential term—their physical interpretation of the many-body interaction term $f(\rho)$ was the tight-binding theory, therefore describing f_ρ to be $\sqrt{\rho}$.

2.3.3 The modified embedded atom method (MEAM)

Originally developed for semiconductors, the modified embedded atom method includes the covalent bonding character in the EAM formalism [13]. It has been extended to cubic materials in [14], and unlike EAM and EAM/FS, the underlying idea is empirical. While in the original EAM, electron densities are assumed to be spherical, MEAM includes gradients in the electron density which represent directional bonding. Additionally, the pair potentials are not assumed to be exclusively repulsive. Being a refined version of the original EAM and having been improved over the years, current MEAM potentials can depict material properties with high accuracy.

2.4   Computational implementation

One of the most common molecular dynamics simulation packages is the open-source code LAMMPS (Large-scale Atomic/Molecular Massively Parallel Simulator)[15]. Although there are numerous packages to perform these simulations, there is a standard "recipe" for molecular dynamics simulations. Before the simulation cell can be set up, some basic conditions for the respective calculation have to be agreed upon. Simplifications to minimize computational effort include boundary conditions, which are usually chosen to be periodic as to mimic a bulk material without having to deal with huge simulation cells, and a potential cutoff to exclude long-range interactions. For any simulation, initial conditions regarding the simulation cell have to be determined: these include the dimensions and shape of the simulation cell, as well as the number of atoms and their positions in the cell. Establishing these initial conditions is pretty straight forward for crystalline solids. Unlike for molecular dynamics simulations, temperature and initial velocities in a molecular statics simulation are zero. For molecular dynamics, a timestep and total simulation time, an integration algorithm/method and an ensemble have to be chosen. These terms and concepts have been described extensively in literature and will not be explained here since they are not used in molecular statics calculations [4].

2.4.1   Potential cutoff and neighbor lists

To allow reasonable computing times, a simplification used in many simulation methods is made. Interatomic potentials approach zero at large distances and including interactions beyond a certain distance uses a lot of computation time while having very little influence on the results. To exclude some of these long-range interactions, the interatomic potential is truncated at a cutoff distance r_c. Cutting of the potential abruptly causes discontinuities in potential and force, which is why there are different approaches to reduce or prevent them by adding a constant potential value or interpolation. The value of the cutoff distance depends on the potential (or bonding) type, but is chosen more or less arbitrarily. However, it must be smaller than half of the primary box size to prevent double interactions of a particle with another particle and its replica.

To limit the calculations to the particles within the cutoff distance, it is necessary to keep track of the atoms possibly interacting with each other. Before the simulation starts, atoms within a certain distance to each other are added to a so-called neighbor list. This distance must be a little larger than the cutoff distance, as atoms move during the simulation and can enter or leave this area and therefore, the list. The list is updated regularly, limiting the calculations to currently listed atoms only [3, 4].

2.4.2   Periodic boundary conditions

A main advantage of MD simulations is that the desired properties or processes can be calculated for bulk materials, although the calculations themselves happen on an atomic level. For this to be possible, the system size does not have to be infinitely large. Instead, a comparably small simulation cell is created and filled with particles. The bulk sample is then modelled by infinite repetition of this cell in space: the boundary conditions applied to the system are periodic. Any property or trajectory associated with a particle within this primary box will be replicated by its equivalent in an image box. This also applies to an atom leaving its respective box and being replaced by its replica from an image box. If the distance between two particles in one box is larger than the distance between one particle in one box and an equivalent other particle in another box, the interaction with the shorter distance is included in the calculations. This concept is called minimum image criterion or convention. It is also important to mention that an image box adjacent to the primary box must not destroy the symmetry of the entire system, i.e. overlaps and gaps must be avoided [3, 4].

2.4.3   Initial conditions

Choosing a model to describe a systems properties as accurately as possible is a crucial step in any simulation. The structure of the model should be as close as possible to one of the real system. This is fairly easy for metals and the crystal structures they usually occur in. By positioning the atoms at their usual positions in the respective lattice and replicating this cell, the initial positions of the particles in the simulation cell can be set. As in any other simulation, the goal is to find a system which is as small as possible while representing the relevant properties of the real system. The minimum number of atoms needed to provide reliable results depends on which property or process will be calculated [3, 4].

3   Simulation setup

3.1   Potentials and potential types

In this thesis, the potential types EAM, EAM/Alloy, EAM/FS and MEAM were used. All of them are derived from similar concepts and should therefore be reasonably comparable. The potentials themselves were developed for different purposes and hence fitted to different properties. They were optimized for pure nickel, nickel-aluminum, nickel-aluminum-cobalt and nickel-aluminum-cobalt-chromium-iron compounds. These potentials can be used for different compound types and crystal structures, based on the species they contain. For this thesis, we chose fcc nickel, body-centered cubic (bcc) β-NiAl (B2) and fcc Ni_3Al (L1$_2$) test compounds. An overview of the potential files used in this thesis with their original filenames as downloaded from the NIST Interatomic Potentials Repository [16–18], and the names used in this thesis for clarity is provided in Table 1.

Original filename and source	This thesis
Ni_u3.eam [8]	Ni1986.eam
niu6.txt [19]	Ni1989.eam
Ni_v2.eam.fs [20]	Ni1987.eam.fs
Ni1_Mendelev_2012.eam.fs [21]	Ni2012.eam.fs
Ni99.eam.alloy [22]	Ni1999.eam.alloy
Ni_Zhou2004.eam.alloy [23]	Ni2004.eam.alloy
Ni_v6_2.0.eam [24]	Ni2016.eam.alloy
NiAl02.eam.alloy [25]	NiAl2002.eam.alloy
NiAl_Mishin_2004.eam.alloy [11]	NiAl2004.eam.alloy
Mishin-Ni-Al-2009.eam.alloy [26]	NiAl2009.eam.alloy
Mishin_updated-Ni-Al-Co-2013.eam.alloy [27]	NiAlCo2015.eam.alloy
FeNiCrCoAl-heaweight.setfl [28]	NiAlCoCrFe2020.eam.alloy
Ni.meam [29]	Ni2003.meam
Ni.meam [30]	Ni2015.meam
Ni.meam [31]	Ni2018.meam
AlNi.meam [32]	NiAl2007.meam
AlNi.meam [33]	NiAl2022.meam
NiAlCo.meam [34]	NiAlCo2015.meam

Table 1: Potential filenames as listed on the NIST Interatomic Potentials Repository together with the original reference and how they are labeled in this thesis.

3.2   Toolkit development

The code used for the calculations was LAMMPS [15], an abbreviation for Large-scale Atomic/Molecular Massively Parallel Simulator. LAMMPS is freely available on the internet (`https://www.lammps.org/`). Using the Python wrapper-class PyLammps [35], Jupyter notebooks with detailed documentation were created. They were based on tests freely available on the internet [36–40] and can be found on my GitHub `https://github.com/celinehalkali/mastersthesis.git`. For this thesis, six properties were evaluated for three phases (fcc Ni, β-NiAl and Ni$_3$Al) of each of the chosen nickel-based potentials: equilibrium lattice parameter, elastic properties, point defect energies, stacking fault energies, surface energies and grain boundary energy. The initialization of the different tests is the same except for the boundary conditions. The implementation of the simulation systems changes for each phase and test, and for the planar defects has to be adjusted for the different orientations, too. After defining the settings for each tests, an energy minimization is performed. Since none of the tests undergo a thermodynamic equilibration, the calculations are molecular statics simulations. After that, the output variables are used to calculate the desired properties.

3.2.1   Lattice properties

The calculation of the equilibrium lattice parameter of a crystal at zero Kelvin using LAMMPS is very simple [36]. A simulation cell with the size of the conventional cell of the compound is sufficient because the boundary conditions are periodic in each of the three directions. The crystal structures (Figure 2) were implemented as follows: a fcc conventional cell with nickel atoms at all four basis positions for pure nickel, a bcc unit cell with a nickel atom at the corner and an aluminum atom at (0.5, 0.5, 0.5) for NiAl and a fcc unit cell with an aluminum atom at the corner and three nickel atoms at the adjacent faces for Ni$_3$Al. To evaluate the equilibrium lattice parameter, neither temperature nor atom velocities are needed. It was obtained via a pressure equilibration, during which the atoms are subject to isotropic pressure, and the system can only undergo a specific change in cell volume. For cubic crystals, the lattice parameter then corresponds to the length of the simulation cell in any dimension after the energy minimization and can be obtained directly, without any need for further calculations. The total energy of the system corresponds to the cohesive energy E_{coh} of each compound, which, together with the equilibrium lattice constant, was used for further calculations.
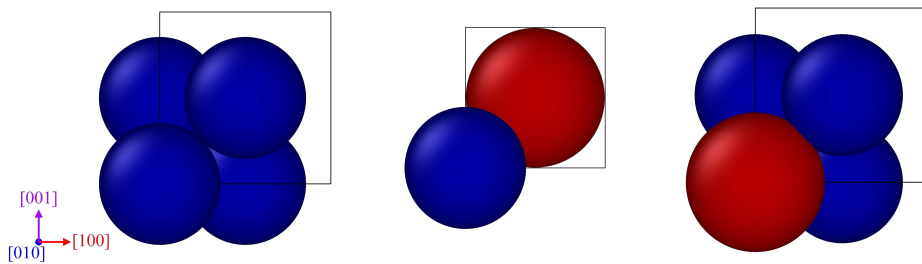
Figure 2: Crystal configuration of fcc Ni (left), β-NiAl (middle) and Ni$_3$Al (right). Nickel atoms are displayed in blue, aluminum atoms in red.

3.2.2 Elastic properties

For the calculation of elastic properties at zero temperature, a direct, deformation-based method using the linear relationship of stress and strain as seen in Hooke's law was applied [41]. The initial reference system was relaxed, and then deformed multiple times: twice in every Voigt's direction, applying a small positive and negative strain each [37]. Upon applying strains in the xy-, yz- and zx- directions, the simulation cell is deformed to a non-orthorhombic cell: This has to be considered in the computational implementation. From the applied strains and their corresponding stress components, the elastic constants can be obtained via Hooke's law:

$$\sigma_i = \sum_j C_{ij}\varepsilon_j, \tag{11}$$

where σ_i denotes a stress component, ε_j a strain component and C_{ij} the corresponding elastic constant in the elastic matrix $\mathbf{C}$:

$$\mathbf{C} = \begin{bmatrix} C_{11} & C_{12} & C_{13} & C_{14} & C_{15} & C_{16} \\ C_{12} & C_{22} & C_{23} & C_{24} & C_{25} & C_{26} \\ C_{13} & C_{23} & C_{33} & C_{34} & C_{35} & C_{36} \\ C_{14} & C_{24} & C_{34} & C_{44} & C_{45} & C_{46} \\ C_{15} & C_{25} & C_{35} & C_{45} & C_{55} & C_{56} \\ C_{16} & C_{26} & C_{36} & C_{46} & C_{56} & C_{66} \end{bmatrix} \tag{12}$$

The cubic lattice symmetry allows some simplifications. In a perfect lattice, the relations $C_{11} = C_{22} = C_{33}$, $C_{12} = C_{13} = C_{23} = C_{21} = C_{31} = C_{32}$ and $C_{44} = C_{55} = C_{66}$ hold true, and all remaining entries are zero. In case there are slight deviations in the calculation results, the values are averaged and only three individual components remain. The resulting

elastic matrix is composed as follows:

$$\mathbf{C} = \begin{bmatrix} C_{11} & C_{12} & C_{12} & 0 & 0 & 0 \\ C_{12} & C_{11} & C_{12} & 0 & 0 & 0 \\ C_{12} & C_{12} & C_{11} & 0 & 0 & 0 \\ 0 & 0 & 0 & C_{44} & 0 & 0 \\ 0 & 0 & 0 & 0 & C_{44} & 0 \\ 0 & 0 & 0 & 0 & 0 & C_{44} \end{bmatrix}. \tag{13}$$

From those three elastic constants, the bulk modulus, K, shear modulus, G, Young's modulus, E, and Poisson's ratio, ν, are obtained. The Voigt [42] and Reuss [43] moduli denote the upper (K_V, G_V) and lower (K_R, G_R) bounds of bulk and shear moduli, respectively. From those, the Voigt-Reuss-Hill averages (K_{VRH}, G_{VRH}) are calculated which lead to good results for bulk and shear modulus, and subsequently Young's modulus and Poisson's ratio [44]. In cubic cells, K_V, K_R and K_{VRH} are identical:

$$K = K_V = K_R = K_{VRH} = \frac{C_{11} + 2\,C_{12}}{3}. \tag{14}$$

The Voigt and Reuss shear moduli have to be obtained separately:

$$G_V = \frac{C_{11} - C_{12} + 3\,C_{44}}{5}, \tag{15}$$

$$G_R = \frac{5\,(C_{11} - C_{12})\,C_{44}}{3\,(C_{11} - C_{12}) + 4\,C_{44}}. \tag{16}$$

From those, the Voigt-Reuss-Hill shear modulus is calculated as follows:

$$G = G_{VRH} = \frac{G_V + G_R}{2}. \tag{17}$$

The Young's modulus, E, and Poisson's ratio, ν, are obtained from the Voigt-Reuss-Hill averaged bulk and shear moduli and follow the relations:

$$E = \frac{9\,KG}{3K + G}, \tag{18}$$

$$\nu = \frac{3K - 2\,G}{2\,(3K + G)}. \tag{19}$$

3.2.3   Point defects

A simulation cell with periodic boundary conditions has been used for the calculation of the point defect formation energies. By comparing the total energy of the perfect simulation cell to the energy of the simulation cell with a point defect, the so-called "raw" point defect energy ε_D is obtained:

$$\varepsilon_D = E_f - E_i, \tag{20}$$

where the point defect D can be a vacancy on sublattice α (V_α) or sublattice β (V_β), or an antisite defect on sublattice α (B_α) or on sublattice β (A_β). However, this "raw" energy does not consider any changes in the composition of the simulation cell and is therefore not universally comparable. An analytical expression for the "effective" vacancy formation energy that does not depend on any reference constants has been derived in [45]:

$$E_f^v(V_\alpha) = \varepsilon_{V_\alpha} + E_{\text{coh}} + \frac{b}{2}(\varepsilon_{A_\beta} - \varepsilon_{B_\alpha}), \tag{21}$$

where α and β describe the respective sublattices, A and B denote an antisite atom of element A or B and V stands for a vacancy. E_{coh} is the cohesive energy of the compound and b is a stoichiometry factor derived from the stoichiometric molecular formula A_nB_m:

$$b = \frac{m}{m + n}. \tag{22}$$

In this study, "effective" vacancy formation energies for a single nickel vacancy have been calculated for pure nickel, NiAl and Ni$_3$Al. For pure nickel, the last term in Equation (21) cancels out because there are no antisite defects in elemental crystals and simplifies to

$$E_f^v(V_{\text{Ni}}) = \varepsilon_{V_{\text{Ni}}} + E_{\text{coh}}. \tag{23}$$

For NiAl, Equation (21) results in

$$E_f^v(V_{\text{Ni}}) = \varepsilon_{V_{\text{Ni}}} + E_{\text{coh}} + \frac{1}{2} \cdot \frac{1}{2} \cdot (\varepsilon_{\text{Ni}_{\text{Al}}} - \varepsilon_{\text{Al}_{\text{Ni}}}) \tag{24}$$

and for Ni$_3$Al in

$$E_f^v(V_{\text{Ni}}) = \varepsilon_{V_{\text{Ni}}} + E_{\text{coh}} + \frac{1}{2} \cdot \frac{1}{4} \cdot (\varepsilon_{\text{Ni}_{\text{Al}}} - \varepsilon_{\text{Al}_{\text{Ni}}}). \tag{25}$$
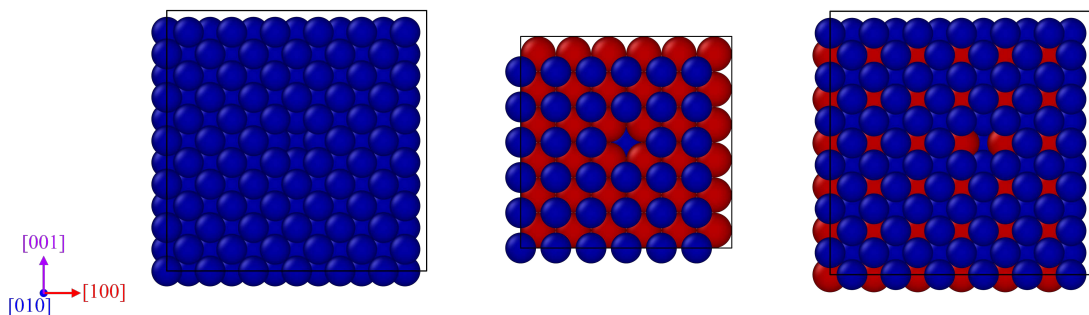
Figure 3: A nickel monovacancy in fcc Ni (left), β-NiAl (middle) and Ni$_3$Al (right).

3.2.4 Planar defects

Three types of planar defect energies have been calculated in this thesis: stacking fault, surface and grain boundary energies. These properties have been evaluated for pure nickel only.

14

The stacking fault energy in fcc metals is typically calculated for the close packed (111) plane. For its evaluation, the z-axis of the simulation cell was chosen to be parallel to the [111] direction of the conventional cell so that the xy-plane corresponds to the (111) plane. This allows for a simple computational implementation of the stacking fault. There are two ways to introduce a stacking fault into a system: for an extrinsic stacking fault, an extra plane has to be inserted, changing the stacking sequence from ABCABCABC to ABCAB**A**CABC, as shown in Figure 4b. An intrinsic stacking fault corresponds to a missing plane and the stacking sequence changes from ABCABCABC to ABCAB_ABC (Figure 4c). To realize those stacking sequences in the simulation setup, specific regions of the cell are shifted with respect to each other; removing or adding a plane would result in a change of the simulation cell size. Calculating the stacking fault energy is identical for both types. The stacking fault energy γ_{sf} results from the difference between the energy of the system containing the stacking fault E_f and the energy of the initial system E_i, divided by the area of the stacking fault A:

$$\gamma_{sf} = \frac{E_f - E_i}{A}. \tag{26}$$
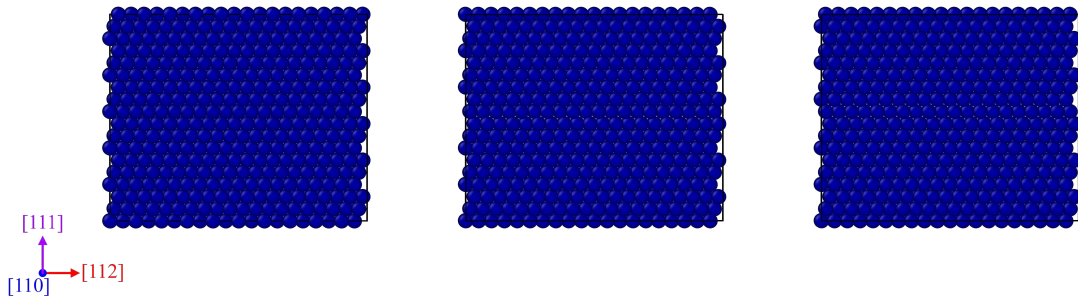
Figure 4: A perfect lattice (left), a lattice with an intrinsic (middle) and a lattice with an extrinsic (right) stacking fault in fcc Ni.

The surface energies of the three low-index surfaces (100), (110) and (111) have been calculated in this thesis. In LAMMPS, defining non-periodic boundary conditions along one axis generates two free surfaces which are normal to this axis. To generate a surface (hkl), the coordinate system was orientated so that the z-axis is parallel to the direction normal to the desired plane. Figure 5 displays the exact orientations for the three simulation cells. Similar to the stacking fault energies, the surface energy γ is the difference between the energy of the system with non-periodic boundary conditions along one axis, E_f ,and the energy of the initial system with periodic boundary conditions in all directions, E_i, divided by two times the surface area, A, because there is a free surface on both sides of the simulation cell:

$$\gamma = \frac{E_f - E_i}{2A}. \tag{27}$$
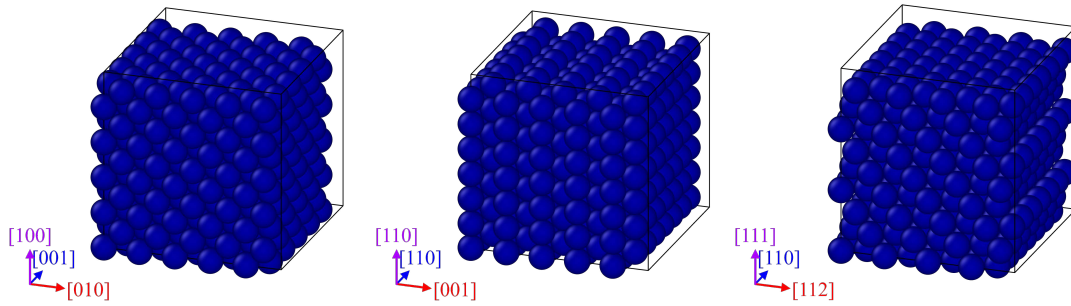
Figure 5: The (100) surface (left), (110) surface (middle) and (111) surface (right) of fcc Ni on top of the respective lattices.

The third planar defect for which the energy has been calculated is a grain boundary. The energy required to create a grain boundary depends on its geometry. Here, a symmetric tilt grain boundary was chosen, where two lattices are misoriented against each other by 36.87° about the [100] rotation axis. This results in a coincidence site lattice where $\Sigma = 5$, meaning that every fifth lattice point is a coinciding point. The boundary conditions for this simulation are periodic in all three directions, resulting in two mirrored, but equivalent grain boundaries within the simulation cell. The simulation cell in Figure 6 shows the two grain boundaries. To calculate the grain boundary energy γ_{gb}, the initial energy of a perfect lattice with the same number of atoms as the cell with the grain boundary is subtracted from the final energy E_f, i.e. the energy of the structure with the grain boundaries. This difference is divided by the grain boundary area (times two, as was just mentioned):

$$\gamma_{gb} = \frac{E_f - E_i}{2A}. \tag{28}$$
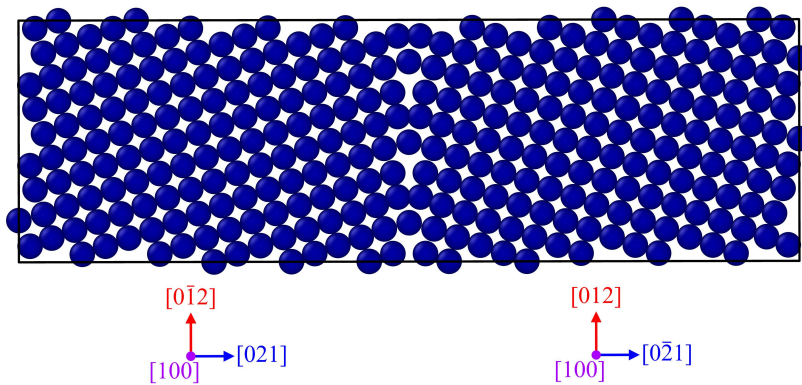
Figure 6: Σ_5 grain boundary of fcc Ni.

4 Results and discussion

In the following six sections, the properties calculated for all eighteen potentials will be compared. Some properties are expected to be met relatively closely by the potentials when they were included in the fitting process. The properties used for the fitting process can be different for each potential and can be practically any material property. Although some of the properties calculated in this thesis have also been used in the parametrization of the potentials, calculating them does not necessarily reproduce the fitting values. However, most of the potentials have been tested for different properties and the results have been published. The results of the tests in this thesis will be compared to the experimental fitting values as well as the calculated results in the papers, if given. If a property has not been included in the potential fitting procedure or calculated and published in the respective paper, an experimental or *ab initio* reference value will be given. Except for the vacancy formation energy, which will be treated separately in Section 4.3, the first-principles values were obtained using projector augmented wave (PAW) pseudopotentials and a generalized gradient approximation as developed in [46] for the exchange and correlation functionals. Tables 3, 4 and 5 show the relative errors of the properties calculated for the three phases (fcc-Ni, β-NiAl and Ni$_3$Al) to the respective DFT reference values (Table 2). These relative errors will be used frequently in the following sections, but will not be referenced individually.

The evaluated properties are the equilibrium lattice parameter, the elastic constants C_{11}, C_{12}, C_{44}, bulk modulus, shear modulus, Young's modulus and Poisson's ratio, the vacancy formation energy for a nickel monovacancy, stacking fault energies of an extrinsic and intrinsic stacking fault, the surface energies for the (100), (110) and (111) surfaces and the grain boundary energy for the Σ_5 symmetric tilt grain boundary. The first three property groups have been calculated for fcc nickel, β-NiAl and Ni$_3$Al phases. The last three properties will be compared for the pure nickel phase only.

The following graphs (Figures 7-18) have different background colors and styles to easily distinguish between the potential types. Different markers differentiate between the material systems the potentials were developed for. All EAM potentials have blue vertical lines as a background, EAM/FS potentials orange cross-hatches, EAM/Alloys green horizontal lines and MEAM potentials purple diagonal lines. All data points from potentials that were developed for pure nickel are shown as empty circles, those for Ni–Al systems as circles where the top half is filled; Ni–Al–Co system potentials are displayed as circles with the left half filled, and the only Ni–Al–Co–Cr–Fe high entropy alloy potential has a filled circle data point.

There are potentials for some material systems that were developed by expanding an existing one. This is the case for the NiAlCo2015.eam.alloy potential, which expands the Ni–Al binary alloy potential of NiAl2009.eam.alloy which bases its nickel potential on the one from NiAl2004.eam.alloy. The same is true for NiAlCo2015.meam, developed on top of the NiAl2007.meam Ni–Al interaction (with one minor change) which itself uses the same nickel interaction parameters as Ni2003.meam. The nickel potential of NiAl2022.meam is based on Ni2015.meam, just as the nickel potential of NiAlCoCrFe2020.eam.alloy is based on Ni1999.eam.alloy. The tests in this thesis are only implemented for pure nickel or Ni–Al compounds and therefore result in the same outcome for both "original" and "extended" potentials. Although running the tests for both potentials seems redundant, it validates that during the "extension", the original potential was preserved. For the remainder of this thesis, they will therefore be discussed together whenever applicable. Another potential that has to be mentioned is the Ni2016.eam.alloy potential. Originally, it was downloaded from the NIST Interatomic Potentials Repository as an EAM potential, but due to the structure of the file and due to the fact that it was partly based on Ni1999.eam.alloy, we have concluded that it can only be used as an EAM/Alloy potential.

Property	a	B	C_{11}	C_{12}	C_{44}	G	E	ν	E_v^f	γ_{sf}^{in}	γ_{sf}^{ex}	$\gamma^{(100)}$	$\gamma^{(110)}$	$\gamma^{(111)}$	E_{gb}
fcc-Ni	3.506	198	276	159	132	95	245	0.29	1.42	129	126	2208	2286	1924	1383
β-NiAl	2.888	162	208	138	117	72	188	0.31	0.74	-	-	-	-	-	-
Ni$_3$Al	3.561	177	238	147	129	85	220	0.29	1.5	-	-	-	-	-	-
Unit	Å	GPa	GPa	GPa	GPa	GPa	GPa	-	eV/atom	mJ/m²	mJ/m²	mJ/m²	mJ/m²	mJ/m²	mJ/m²

Table 2: DFT reference values for all properties evaluated in this thesis.

Property	a	B	C_{11}	C_{12}	C_{44}	G	E	ν	E_v^f	γ_{sf}^{in}	γ_{sf}^{ex}	$\gamma^{(100)}$	$\gamma^{(110)}$	$\gamma^{(111)}$	E_{gb}
Ni1986.eam	0.4	−8.8	−15.5	−3.0	−3.3	−15.9	−14.7	5.9	14.9	−88.9	−88.6	−28.9	−24.8	−25.4	−0.6
Ni1989.eam	0.4	−8.8	−14.6	−3.7	1.1	−12.1	−11.4	3.3	20.2	−88.2	−87.9	−26.4	−22.2	−22.4	3.4
Ni1987.eam.fs	0.5	−5.4	−5.5	−5.3	−0.4	−2.4	−2.5	−0.9	0.2	−80.7	−80.0	−34.3	−27.8	−29.0	−5.3
Ni2012.eam.fs	0.3	−8.8	−10.5	−7.4	−7.0	−10.0	−9.5	1.9	23.8	50.8	56.0	−36.4	−30.7	−33.4	18.6
Ni1999.eam.alloy	0.4	−8.5	−10.2	−7.0	−5.4	−8.9	−8.6	1.4	12.7	−2.9	0.8	−14.9	−10.4	−15.3	13.1
Ni2004.eam.alloy	0.4	−8.8	−10.5	−7.3	−5.4	−9.1	−8.8	1.3	19.0	−23.6	−20.3	−15.3	−9.8	−7.1	−8.0
Ni2016.eam.alloy	0.4	−8.8	−12.7	−5.4	−3.7	−11.5	−10.9	3.0	10.7	4.4	7.6	−12.3	−8.7	−8.6	−2.3
NiAl2002.eam.alloy	−1.5	113.2	130.1	98.6	3.1	52.7	59.4	19.3	−60.2	177.0	206.7	−42.2	−35.0	−44.4	−30.4
NiAl2004.eam.alloy	0.4	−8.6	−12.6	−5.1	−3.5	−11.4	−10.8	3.0	10.7	4.4	7.6	−12.3	−8.7	−8.6	−2.3
NiAl2009.eam.alloy	0.4	−8.6	−12.6	−5.2	−3.5	−11.4	−10.8	3.0	10.7	4.4	7.6	−12.3	−8.7	−8.6	−2.3
NiAlCo2015.eam.alloy	0.4	−8.6	−12.6	−5.1	−3.5	−11.4	−10.8	3.0	10.7	4.4	7.6	−12.3	−8.7	−8.6	−2.3
NiAlCoCrFe2020.eam.alloy	0.4	−8.5	−10.1	−7.0	−5.3	−8.8	−8.5	1.3	12.7	−2.9	0.8	−14.9	−10.4	−15.3	13.1
Ni2003.meam	0.4	−5.3	−5.4	−5.2	−0.2	−2.2	−2.3	−0.9	6.2	−3.5	−0.8	−12.3	−11.1	−16.9	0.6
Ni2015.meam	0.4	−5.4	−5.6	−5.2	−0.8	−2.7	−2.8	−0.6	−16.2	−48.5	−47.1	−18.0	−19.0	−22.5	−15.2
Ni2018.meam	0.4	−4.6	−7.5	−2.0	−1.6	−6.9	−6.4	2.6	−5.4	−57.9	−56.7	−24.3	−24.4	−24.3	−14.7
NiAl2007.meam	0.4	−5.3	−5.4	−5.2	−0.2	−2.2	−2.3	−0.9	6.2	−3.5	−0.8	−12.3	−11.1	−16.9	0.6
NiAl2022.meam	0.4	−5.4	−5.6	−5.2	−0.8	−2.7	−2.8	−0.6	−16.9	−48.5	−47.2	−22.0	−23.0	−25.5	−15.6
NiAlCo2015.meam	0.4	−5.3	−5.4	−5.2	−0.2	−2.2	−2.3	−0.9	6.2	−3.5	−0.8	−12.3	−11.1	−16.9	0.6

Table 3: Relative error of all evaluated properties for the pure nickel phase (fcc Ni) to the respective DFT reference values in percent.

19

Property	a	B	C_{11}	C_{12}	C_{44}	G	E	ν	E_v^f
NiAl2002.eam.alloy	-1.0	-1.4	-3.9	1.2	2.6	-3.7	-3.3	0.1	-39.4
NiAl2004.eam.alloy	-1.0	46.1	43.0	49.5	45.8	40.1	41.0	1.1	33.9
NiAl2009.eam.alloy	-1.9	-1.9	-8.2	3.6	3.8	-10.6	-9.5	3.7	19.5
NiAlCo2015.eam.alloy	-1.9	-1.9	-8.3	3.5	3.8	-10.6	-9.5	3.7	19.5
NiAlCoCrFe2020.eam.alloy	4.0	-15.9	-11.7	-18.4	-20.3	-12.0	-12.4	-3.6	-26.7
NiAl2007.meam	-0.4	-2.5	-3.3	-1.2	4.5	0.2	-0.1	-2.6	0.6
NiAl2022.meam	9.8	-21.2	-21.8	-20.1	-19.7	-21.5	-21.4	-0.9	81.6
NiAlCo2015.meam	-0.4	-2.5	-3.3	-1.2	4.5	0.2	-0.1	-2.6	0.6

Table 4: Relative error of all evaluated properties for the β-NiAl phase (B2) to the respective DFT reference values in percent.

Property	a	B	C_{11}	C_{12}	C_{44}	G	E	ν	E_v^f
NiAl2002.eam.alloy	-1.0	39.7	19.4	55.6	-18.3	-27.1	-22.0	32.5	-50.0
NiAl2004.eam.alloy	0.3	2.6	-0.8	5.0	-1.5	-5.0	-4.1	5.6	8.2
NiAl2009.eam.alloy	-0.8	7.5	0.1	13.2	0.9	-8.3	-6.5	10.3	4.7
NiAlCo2015.eam.alloy	-0.8	7.5	0.1	13.2	0.9	-8.3	-6.5	10.3	4.7
NiAlCoCrFe2020.eam.alloy	0.4	-39.1	-16.2	-57.7	11.9	26.0	9.7	-56.2	-26.2
NiAl2007.meam	0.3	2.8	8.2	-2.0	1.7	10.3	9.1	-3.4	-5.7
NiAl2022.meam	7.6	-8.8	-6.2	-11.3	-23.4	-14.1	-13.5	4.6	-59.4
NiAlCo2015.meam	0.3	2.8	8.2	-2.0	1.7	10.3	9.1	-3.4	-5.7

Table 5: Relative error of all evaluated properties for the Ni$_3$Al phase (L1$_2$) to the respective DFT reference values in percent.

4.1 Equilibrium lattice parameter

The results of the first test, the equilibrium lattice parameter, are displayed in Figure 7. It is one of the properties used as input parameter for potential development and the results should therefore show minimum deviation from the values that were used. Since only experimental lattice parameters were used in the potential developments, the results are not expected to match the DFT reference value perfectly.

In Figure 7a, the calculated equilibrium lattice parameters for pure nickel are shown. They are all significantly higher than the DFT value of 3.506 Å [47, 48], but match the experimental values given in the respective papers [8, 11, 19, 22–24, 26–34]. The two EAM/FS potentials deviate from most of the other results, but match the values that have been calculated in [20] and [21]. The only potential leading to a value deviating strongly from the rest of the results is NiAl2002.eam.alloy. This potential has been developed by

fitting the potential to properties of β-NiAl, thus not leading to reasonable results for pure nickel. However, the calculated value is the same as the one given in [25].

Figure 7b shows the results for the equilibrium lattice parameter of β-NiAl, for which the DFT value is 2.888 Å [47, 49]. All potentials except NiAlCoCrFe2020.eam.alloy and NiAl2022.meam are lower than, but reasonably close to the DFT value, with a deviation of less than 2 % for each of them. NiAl2002.eam.alloy results in the value given in [25] which is just 1 % lower than the DFT value. The value obtained with NiAl2004.eam.alloy is very close to the DFT value. Although originally optimized for Ni$_3$Al, structural information from *ab initio* calculations has been included in the fitting database, possibly leading to more accurate results for other compounds than the potential was originally designed for. NiAl2009.eam.alloy and NiAlCo2015.eam.alloy result in the same values as the ones calculated in [26] and [27]. NiAlCoCrFe2020.eam.alloy results in a very high lattice parameter of 3.002 Å, probably because it was fitted to properties of random mixtures of binary systems. NiAl2007.meam and NiAlCo2015.meam result in a lattice parameter of 2.877 Å, deviating from the DFT reference by less than 0.5 %. NiAl2022.meam deviates strongly from both the DFT as well as the experimental fitting value given in [33], and predicts a result of 3.171 Å.

The results for the equilibrium lattice parameter of Ni$_3$Al are displayed in Figure 7c and compared to the DFT value of 3.562 Å [47, 50]. NiAl2002.eam.alloy, developed for β-NiAl, leads to a very low value of 3.526 Å. NiAl2004.eam.alloy matches the experimental value given in the paper which was to be expected because the potential was developed for this compound, and is slightly higher than the DFT value. The two EAM/Alloy potentials NiAl2009.eam.alloy and NiAlCo2015.eam.alloy result in a lower value than the DFT one, but match the results in [26] and [27]. The result for NiAlCoCrFe2020.eam.alloy exceeds the DFT value by less than 0.5 %. It is able to predict the properties of this phase better than for the β-NiAl phase, probably due to the higher nickel content of this compound. NiAl2007.meam and NiAlCo2015.meam result in marginally higher values (0.3 %) than the DFT values, and also deviate slightly from 3.567 Å, given in [32]. The NiAl2022.meam potential does not lead to a satisfactory result as it is 7.6 % higher than the DFT value.
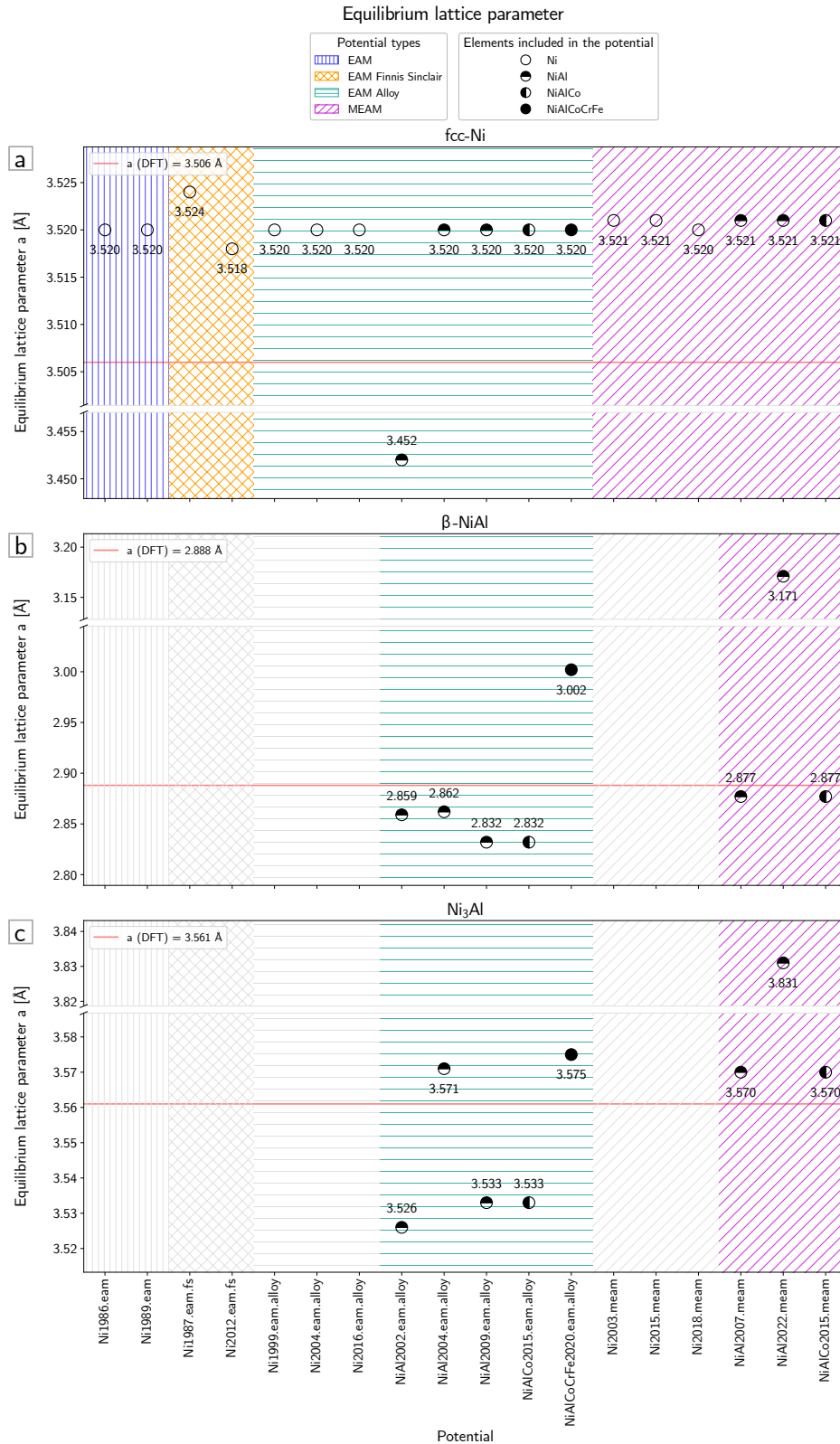
Figure 7: Equilibrium lattice parameter a for a) the pure nickel phase (fcc Ni) of each potential, and b) the β-NiAl and c) the Ni$_3$Al phase of all potentials developed for alloy systems. The red line marks the reference value from DFT. The y-axes are broken to cover the range of all calculated values.

4.2 Elastic properties

4.2.1 Single crystalline elastic constants

In the following three figures (Figures 8, 9 and 10), the three elastic constants, C_{11}, C_{12} and C_{44}, are shown for pure fcc nickel, β-NiAl, and Ni$_3$Al, respectively.

In Figure 8a, the results for C_{11} of pure nickel are compared to the DFT value of 276 GPa [47, 48, 51]. Both EAM potentials are about 15 % lower than the DFT value, and do not match the experimental value either. Ni1987.eam.fs leads to a result only 5.5 % lower than the DFT value, while Ni2012.eam.fs underestimates it by 10.5 %. Ni1999.eam.alloy, Ni2004.eam.alloy and NiAlCoCrFe2020.eam.alloy underestimate the *ab initio* value by a little more than 10 %, but match the experimental input very well. Ni2016.eam.alloy, NiAl2004.eam.alloy, NiAl2009.eam.alloy and NiAlCo2015.eam.alloy fall short of the DFT value by nearly 13 %, underestimating the experimental values, too. NiAl2002.eam.alloy overestimates C_{11} by more than 100 %, possibly due to its optimization to fit the β-NiAl phase. The MEAM potentials are fitted to a higher experimental bulk modulus than most other potentials (see Equation (14) for the relation between C_{11} and B). They underestimate the DFT value by about 5.5 % (except Ni2018.meam which is 7.5 % lower), yielding the closest results to the DFT value in this thesis.

The elastic constant C_{11} for the β-NiAl phase, as displayed in Figure 8b, is compared to the DFT value of 208 GPa [47, 49, 51]. NiAl2002.eam.alloy leads to a good result of 200 GPa. NiAl2004.eam.alloy overestimates this property by 43 %, presumably because it was fitted to pure nickel and Ni$_3$Al properties only. NiAl2009.eam.alloy and NiAlCo2015.eam.alloy, optimized for β-NiAl and Ni$_3$Al properties, result in values more than 8 % lower than the DFT reference, and are also lower than their experimental input. NiAlCoCrFe2020.eam.alloy leads to a value 12 % lower than the DFT value. NiAl2007.meam and NiAlCo2015.meam yield results that are just 3 % lower than the DFT value. The result for NiAl2022.meam is nearly 22 % lower than the DFT value, and is also lower than the value given in [33].

Figure 8c shows C_{11} for the Ni$_3$Al phase, with a DFT reference value of 238 GPa [47, 50, 51]. As expected, NiAl2002.eam.alloy overestimates C_{11} by nearly 20 %. NiAl2004.eam.alloy, NiAl2009.eam.alloy and NiAlCo2015.eam.alloy yield results matching the DFT reference almost exactly. NiAlCoCrFe2020.eam.alloy leads to a value 16 % lower than the DFT value, again probably due to the different parametrization. NiAl2007.meam and NiAlCo2015.meam result in higher values than the experimental one, exceeding the DFT value by 8 %. The result for NiAl2022.meam is lower than the DFT value and does not match the value in [33].
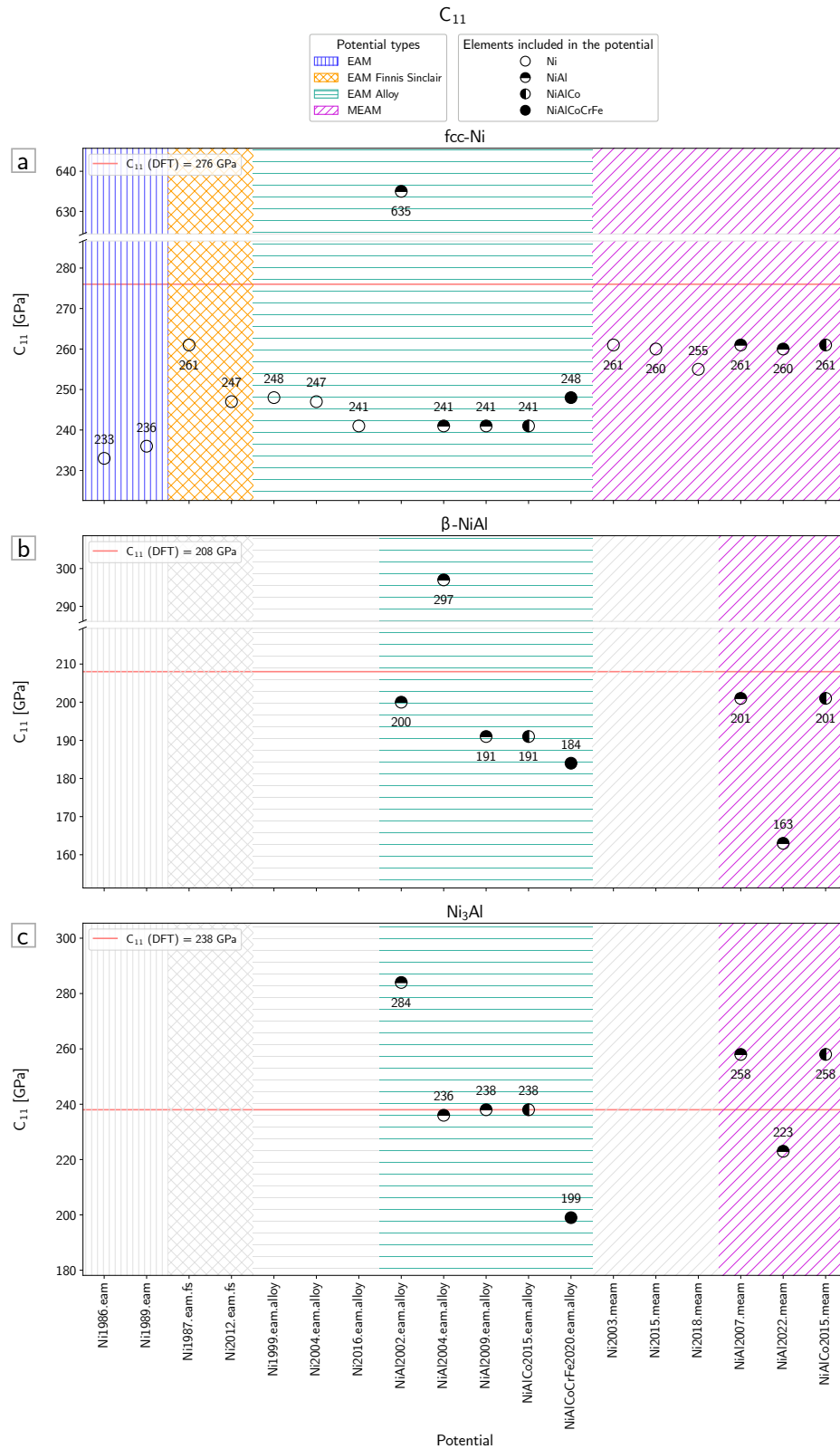
Figure 8: C_{11} for the pure nickel phase (fcc Ni) of each potential, and the β-NiAl and the Ni$_3$Al phase of all potentials developed for alloy systems. The red line marks the reference value from DFT. The y-axes are broken to cover the range of all calculated values.

Figure 9a shows the results for C_{12} for the pure nickel phase of each potential. In this case, the reference value from *ab initio* methods is 159 GPa [47, 48, 51]. Both EAM potentials overestimate the experimental values slightly, and are less than 4 % lower than the DFT reference. Ni1987.eam.fs and Ni2012.eam.fs underestimate the DFT value by 5 and 7 %, respectively. Ni1999.eam.alloy and Ni2004.eam.alloy result in values close to the experimental one and are 7 % lower than the DFT value, while Ni2016.eam.alloy falls short of it by only 5 %. Similar to C_{11}, NiAl2002.eam.alloy is not able to calculate pure nickel properties, exceeding the DFT value by nearly 100 %. NiAl2004.eam.alloy, NiAl2009.eam.alloy and NiAlCo2015.eam.alloy overestimate the experimental input value slightly, and underestimate the DFT reference by 5 %. NiAlCoCrFe2020.eam.alloy reproduces the experimental input, but is 7 % lower than the DFT value. All MEAM potentials except Ni2018.meam yield practically the same values, matching their experimental input, but not the result obtained with *ab initio* methods, underestimating it by 5 %. The result for Ni2018.meam is very good, being only 2 % lower than the DFT value.

The results for C_{12} for the β-NiAl phase (Figure 9b) are compared to a reference value of 138 GPa, calculated with *ab initio* methods [47, 49, 51]. The result obtained with NiAl2002.eam.alloy is very close to the experimental input as well as the DFT value, exceeding it by just over 1 %. NiAl2004.eam.alloy overestimates the DFT value by nearly 50 %. NiAl2009.eam.alloy and NiAlCo2015.eam.alloy match the DFT value well, overestimating it by less than 4 %, while NiAlCoCrFe2020.eam.alloy produces a predicts a value 18 % lower than the *ab initio* reference. The results for NiAl2007.meam, and consequently NiAlCo2015.meam, match the experimental input very well, and are only 1 % lower than the DFT value. NiAl2022.meam leads to a very low value, falling short of the DFT value by 20 %.

The results for C_{12} for the Ni_3Al phase can be found in Figure 9c. The reference value obtained with first-principles methods is 147 GPa [47, 50, 51]. As expected, the result from NiAl2002.eam.alloy does not match the DFT value at all, overestimating it by more than 55 %. NiAl2004.eam.alloy yields a result 5 % higher than the DFT value, and predicts the experimental input reasonably well. NiAl2009.eam.alloy and NiAlCo2015.eam.alloy lead to higher results than the experimental input and the *ab initio* value, exceeding it by 13 %. The NiAlCoCrFe2020.eam.alloy potential results in a value less than half of the DFT reference. The two related MEAM potentials, NiAl2007.meam and NiAlCo2015.meam, yield lower results than the experimental input, underestimating the DFT value by only 2 %. NiAl2022.meam underestimates C_{12} by 11 %.
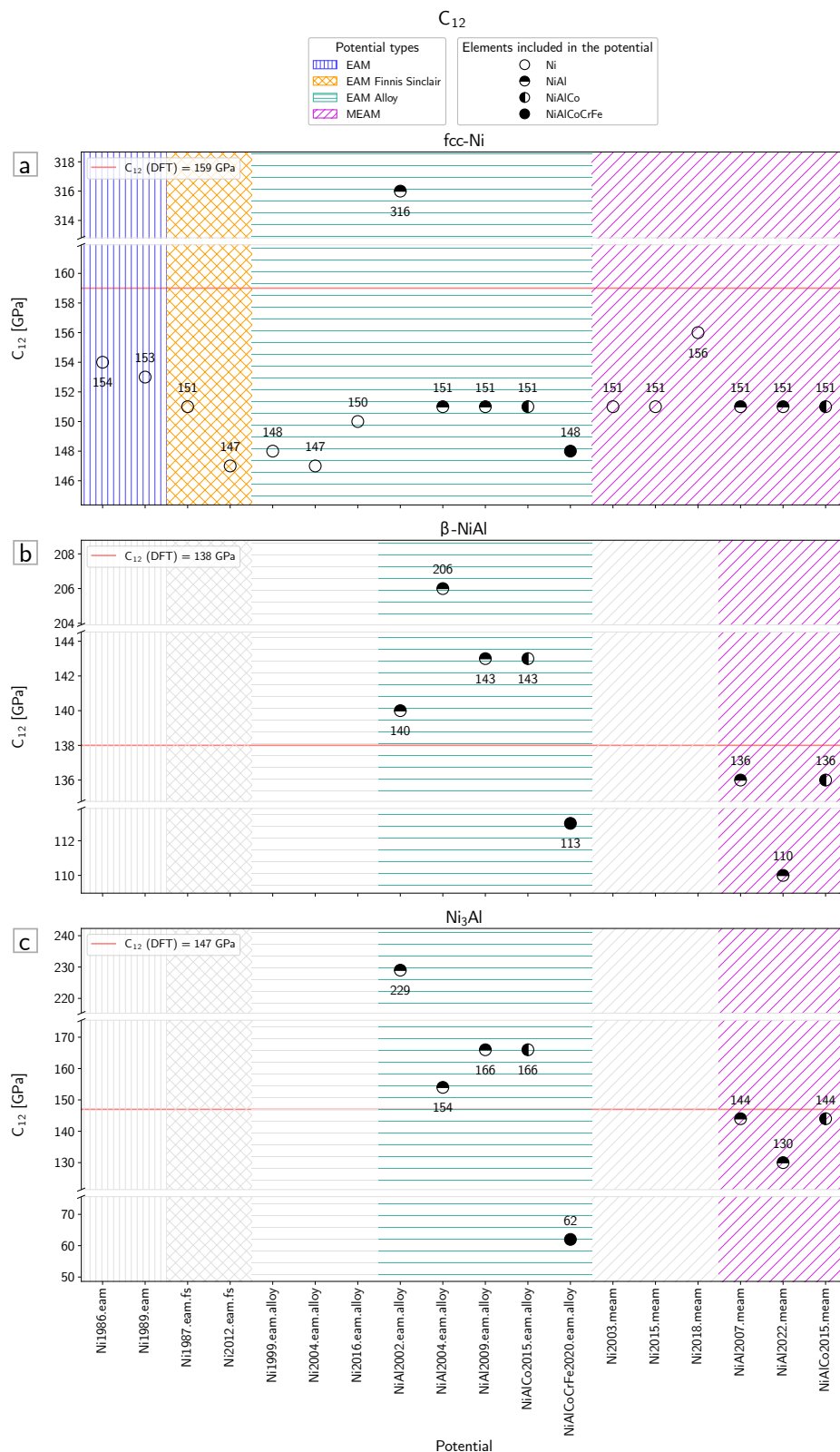
Figure 9: C_{12} for a) the pure nickel phase (fcc Ni) of each potential, and b) the β-NiAl and c) the Ni$_3$Al phase of all potentials developed for alloy systems. The red line marks the reference value from DFT. The y-axes are broken to cover the range of all calculated values.

The results for C_{44} for the pure nickel phase of all potentials will be compared to the DFT value of 132 GPa [47, 48, 51] and are shown in Figure 10a. Most of the calculated values are in close range to the *ab initio* reference, as the value used for potential development are mostly very close to it. While Ni1986.eam underestimates both the input value and the DFT value, Ni1989.eam underestimates the input, but matches the DFT reference well, overestimating it by just 1 %. Ni1987.eam.fs matches the DFT value almost exactly (-0.4 %), contrary to Ni2012.eam.fs which leads to the lowest result of all potentials (-7 %). All results calculated with EAM/Alloy potentials agree well with the input values as well as the DFT reference, all underestimating it by less than 6 %, except for NiAl2002.eam.alloy which exceeds it by 3 %. This result is very good, especially when compared to the other two elastic constants. Most of the MEAM potentials were fitted to a higher input value which corresponds to the reference value. Ni2018.meam shows a deviation of -1.6 %, while all other results deviate from the first-principles result by less than 1 %.

In Figure 10b, the values obtained for C_{44} of the β-NiAl phase are shown. They are compared to the DFT value of 117 GPa [47, 49, 51]. Only two of the potentials (NiAl2002.-eam.alloy and NiAl2009.eam.alloy) were fitted to C_{44} of β-NiAl. Both of them, and therefore also NiAlCo2015.eam.alloy, lead to marginally higher results (less than 4 %) than the input as well as the DFT value. The DFT reference was exceeded by nearly 46 % with the result obtained with NiAl2004.eam.alloy. This was to be expected as it was optimized for the Ni$_3$Al phase. Again, NiAlCoCrFe2020.eam.alloy leads to an imprecise result due to its fitting parameters for the binary phases, underestimating the DFT value by 20 %. NiAl2022.meam predicts a similar value and is therefore also significantly lower than the reference value. The two other MEAM potentials lead to satisfactory results that are a bit higher than the input value, and exceed the DFT value by less than 5 %.

In Figure 10c, C_{44} of the Ni$_3$Al phase is shown for each potential. The first-principles reference value for C_{44} is 129 GPa [47, 50, 51]. As for the other two elastic constants, the NiAl2002.eam.alloy potential does not result in a value close to the DFT value, underestimating it by 18 %. NiAlCoCrFe2020.eam.alloy yields a result 12 % higher than the *ab initio* reference. The other three EAM/Alloy potentials yield lower results than the experimental fitting parameters, and deviate from the DFT reference by less than 2 %. NiAl2007.meam and NiAlCo2015.meam also yield good results that fit both the input as well as the DFT reference well. Similar to β-NiAl, NiAl2022.meam underestimates the DFT value distinctly, by 23 %.
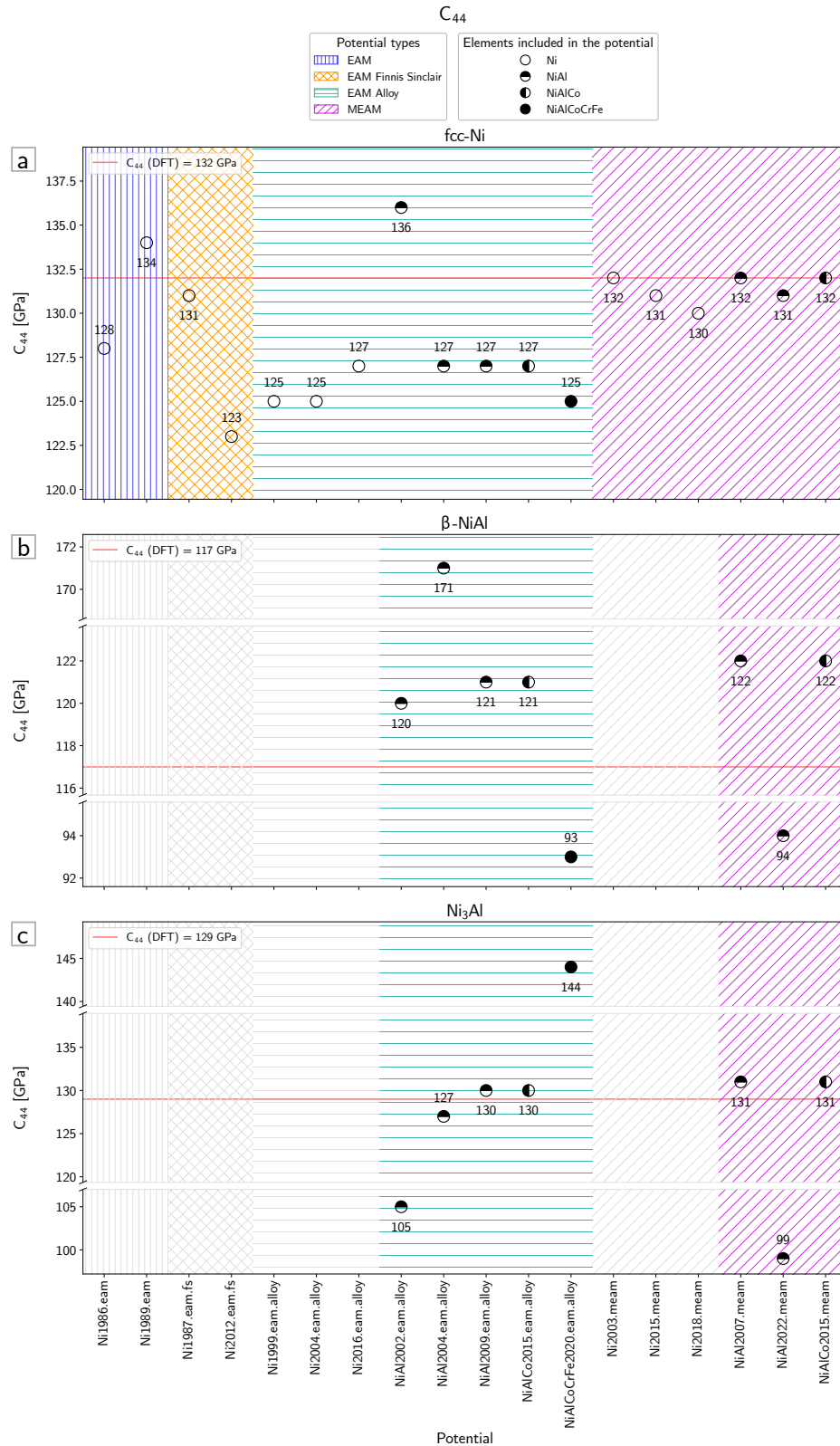
Figure 10: C_{44} a) for the pure nickel phase (fcc Ni) of each potential, and b) the β-NiAl and c) the Ni$_3$Al phase of all potentials developed for alloy systems. The red line marks the reference value from DFT. The y-axes are broken to cover the range of all calculated values.

4.2.2 Bulk modulus

Just like the equilibrium lattice parameter, the bulk modulus is used as an input parameter in the potential development and should match the experimental input values instead of the DFT reference value. As described in Section 3, the bulk modulus is a function of the two elastic constants C_{11} and C_{12} (c.f. Equation (14)).

The DFT reference value for pure nickel is 198 GPa, as found in [47, 48, 51]. The results for the bulk modulus for the pure nickel phase of all potentials can be found in Figure 11a. NiAl2002.eam.alloy, which was fitted purely to properties of the β-NiAl phase, results in a value more than twice as high as any experimental or first-principles value. All other potentials match their experimental input value very well. Therefore, the results for the bulk modulus are all lower than the *ab initio* value and none of the potentials is able to calculate values deviating by less than 10 % from the DFT value of the pure nickel phase.

In Figure 11b, the bulk moduli of the β-NiAl phase are compared with the *ab initio* reference of 162 GPa [47, 49, 51]. The NiAl2002.eam.alloy potential reproduces the experimental input value very well, as well as the DFT value which itself is very close to the experimental one used for this potential. Again, NiAl2004.eam.alloy overestimates the DFT value significantly, by 46 %, while NiAl2009.eam.alloy and NiAlCo2015.eam.alloy agree well with it. Following the trend observed for the elastic constants, NiAlCoCrFe2020.eam.alloy and NiAl2022.meam yield very low values, falling short of the DFT reference by 16 and 21 %, respectively. The other two MEAM potentials, NiAl2007.meam and NiAlCo2015.meam, agree well with the input values and hence the DFT reference, as the experimental values are only slightly lower than the *ab initio* reference value.

Figure 11c shows the bulk moduli calculated for the Ni$_3$Al phase which are compared to the DFT value of 177 GPa [47, 50, 51]. The two potentials that where optimized for different compounds (NiAl2002.eam.alloy and NiAlCoCrFe2020.eam.alloy) deviate strongly from the *ab initio* value, the former overestimating, the latter underestimating it by 40 %. NiAl2004.eam.alloy, optimized specifically for this phase, agrees well with its experimental input and the DFT reference, exceeding it by less than 3 %. NiAl2009.eam.alloy and NiAlCo2015.eam.alloy lead to slightly higher results but are not far off of both the experimental input and the first-principles reference. NiAl2007.meam and NiAlCo2015.meam predict the experimental value perfectly, and hence overestimate the DFT value by less than 3 %. NiAl2022.meam underestimates the bulk modulus by 9 %, yielding a significantly better result than for the β-NiAl phase.
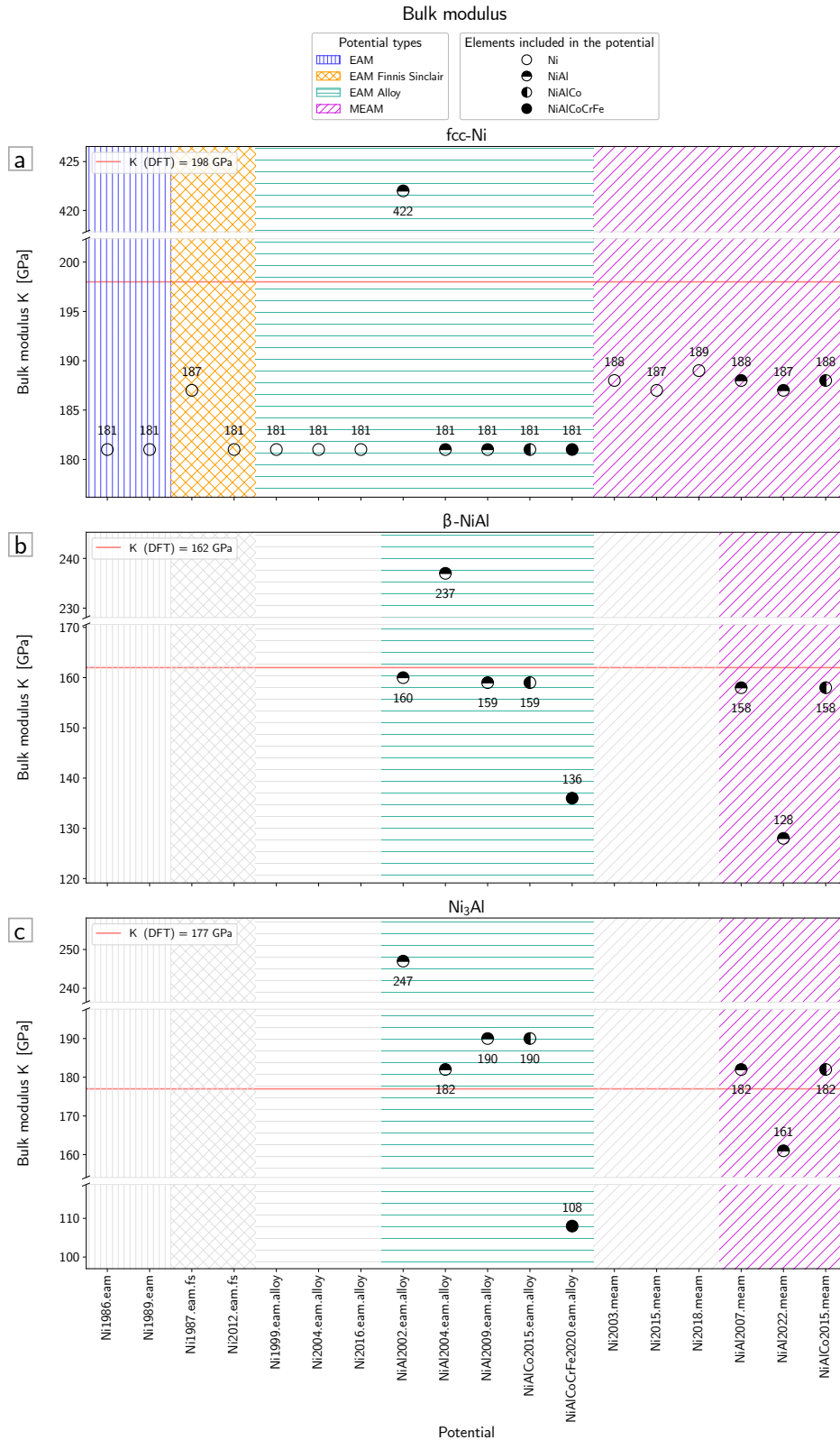
Figure 11: Bulk modulus K for a) the pure nickel phase (fcc Ni) of each potential, and b) the β-NiAl and c) the Ni$_3$Al phase of all potentials developed for alloy systems. The red line marks the reference value from DFT. The y-axes are broken to cover the range of all calculated values.

4.2.3   Shear modulus

Contrary to the bulk modulus, the shear modulus of a material is not directly used during potential development. However, it is calculated as described in Equations (15), (16) and (17) and is thus a function of the three elastic constants. Therefore, the shear modulus calculated with the values used during potential development will be referred to as "input value" for simplicity. Due to the calculation of the shear modulus, similar trends as those observed for C_{11}, C_{12} and C_{44} should be present for this property.

Figure 12a shows the calculated values for pure nickel. The DFT reference for the shear modulus of pure nickel is 95 GPa [47, 48, 51]. Ni1986.eam and Ni1989.eam fall short of the DFT reference (by 16 and 12 %, respectively) as well as the input value. Ni1987.eam.fs leads to a very good result, only showing minimum deviation from the DFT value. Ni2012.eam.fs, as well as all EAM/Alloy potentials except NiAl2002.eam.alloy yield results between 9 and 12 % lower than the *ab initio* reference, but matching their input value well. As for all other properties, the result obtained with NiAl2002.eam.alloy is very far off the desired value, overestimating it by more than 50 %. The input value generally used for the MEAM potentials was close to the DFT value and the results obtained with those potentials are therefore very close to the reference, all underestimating it by less than 3 %. Only Ni2018.meam yields a result that is 7 % lower than the DFT value.

The calculated shear moduli of the β-NiAl phase are illustrated in Figure 12b and compared to the *ab initio* reference value 72 GPa [47, 49, 51]. NiAl2002.eam.alloy yields its input value, which is just 4 % lower than the DFT value. NiAl2004.eam.alloy leads to a very high result, overestimating the DFT value by 40 %. NiAl2009.eam.alloy and NiAlCo2015.eam.alloy, as well as NiAlCoCrFe2020.eam.alloy, yield lower values than the input value and hence the DFT reference. The results obtained with NiAl2007.meam and NiAlCo2015.meam are slightly higher than the input and match the DFT value almost exactly. The value obtained with NiAl2022.meam is more than 21 % lower than the first-principles result.

For the Ni$_3$Al phase, the results are compared to the DFT value of 85 GPa [47, 50, 51] and are shown in Figure 12c. The result obtained with NiAl2002.eam.alloy is 27 % lower than the DFT reference, while the one obtained with NiAl2004.eam.alloy corresponds well to the input value and is only 5 % lower than the DFT value. NiAl2009.eam.alloy and NiAlCo2015.eam.alloy yield lower results than the input value and are 8 % lower than the DFT value. The shear modulus calculated with NiAlCoCrFe2020.eam.alloy is very high, exceeding the *ab initio* reference by 26 %. NiAl2007.meam and NiAl2022.meam result in a value 10 % higher than the DFT value, and also higher than the input value. NiAl2022.meam predicts a result 14 % lower than the first-principles reference.
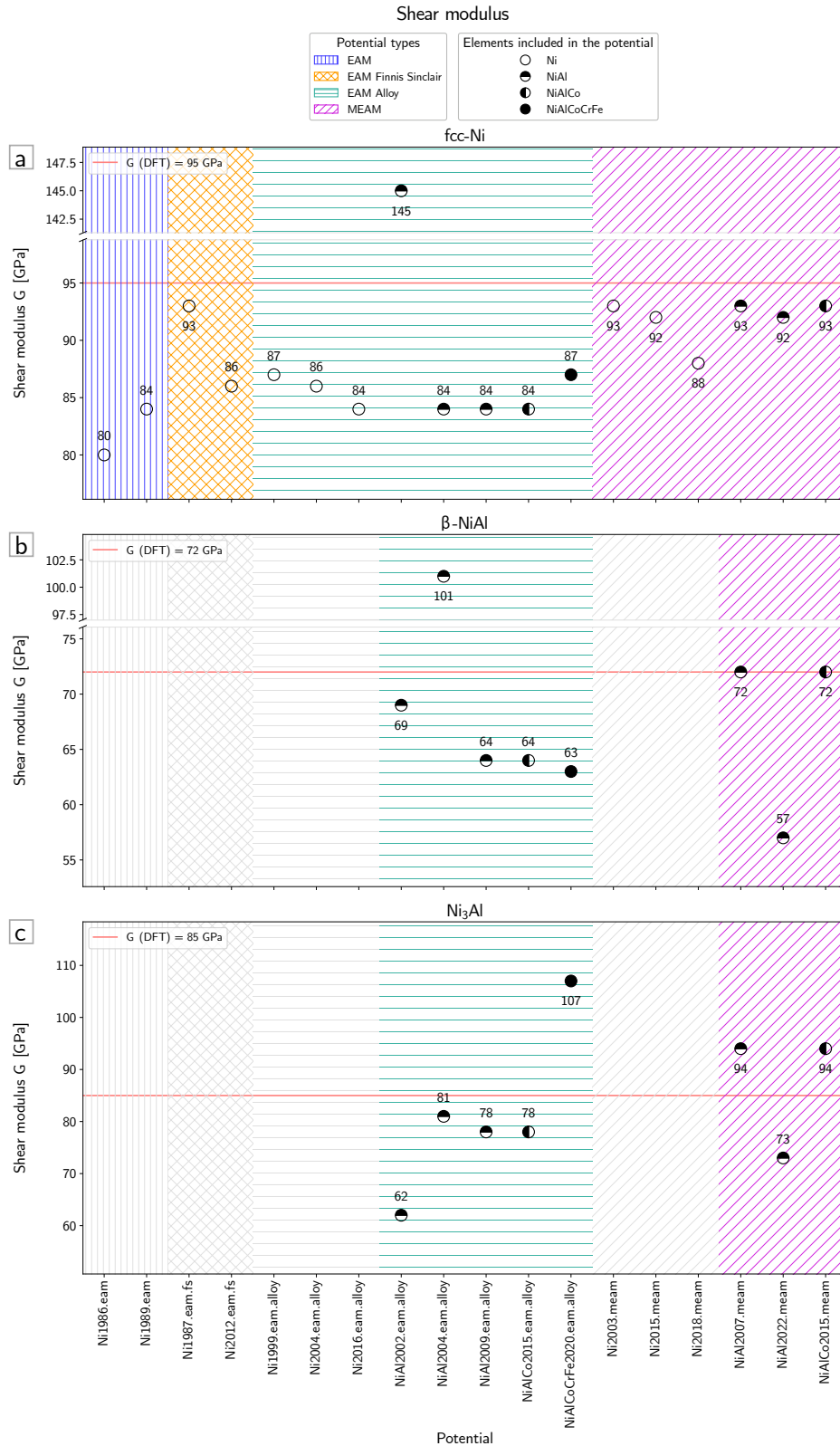
Figure 12: Shear modulus G for a) the pure nickel phase (fcc Ni) of each potential, and b) the β-NiAl and c) the Ni$_3$Al phase of all potentials developed for alloy systems. The red line marks the reference value from DFT. The y-axes are broken to cover the range of all calculated values.

4.2.4 Young's modulus

The Young's modulus is the third property in this thesis that is calculated from the three elastic constants, as seen in Equation (18). Just like the shear modulus, it was not used as a potential fitting parameter but will follow similar trends as those seen for the elastic constants. Again, the "input value" is the one calculated with the elastic constants the potential was fitted to.

The Young's moduli for pure nickel are compared with the first-principles reference value of 245 GPa [47, 48, 51] and are displayed in Figure 13a. Ni1986.eam leads to a very low value, falling short of the DFT value by 15 %. Although the result calculated with Ni1989.eam is a little higher, it is still 11 % lower than the *ab initio* reference. Ni1987.eam.fs yields a result that is just 2.5 % lower than the DFT reference. Ni2012.eam.fs as well as all EAM/Alloy potentials (except NiAl2002.eam.alloy which yields a very elastic modulus) give results that are close to the input value, underestimating it roughly 10 % . All MEAM potentials except Ni2018.meam lead to results very close to the DFT value, never deviating from it by more than 3 %. Ni2018.meam yields a result that is 6 % lower than the DFT value. Only if high values for the elastic constants were used for potential development, the results for the Young's modulus were satisfactory.

In Figure 13b, the results for the Young's moduli for the β-NiAl phase are shown. The DFT value they are compared to is 188 GPa [47, 49, 51]. NiAl2002.eam.alloy predicts a Young's modulus that is just 3 % lower than the *ab initio* value. With NiAl2004.eam.alloy, the Young's modulus is overestimated by 41 %. NiAl2009.eam.alloy, NiAlCo2015.eam.alloy and NiAlCoCrFe2020.eam.alloy yield 9.5, 9.5 and 12.4 % lower results than the DFT value. NiAl2007.meam and NiAlCo2015.meam predict the DFT value. Contrarily to that, NiAl2022.meam results in the lowest result of all potentials (21 % lower than the DFT reference).

Figure 13c shows the results obtained for the Young's moduli of the Ni$_3$Al phase. The reference value from the first-principles methods is 220 GPa [47, 50, 51]. Similar to the previous properties, the Young's modulus calculated with NiAl2002.eam.alloy deviates significantly from the *ab initio* value. While NiAl2004.eam.alloy predicts the best result, it is still 4 % lower than the DFT value. NiAl2009.eam.alloy and NiAlCo2015.eam.alloy are even further off (-6.5 %), while NiAlCoCrFe2020.eam.alloy yields a 10 % higher value than the desired DFT reference. The first and third MEAM potential give similar results, overestimating the first-principles result by 9 %. NiAl2022.meam predicts a very low Young's modulus value, although not as far off as NiAl2002.eam.alloy.
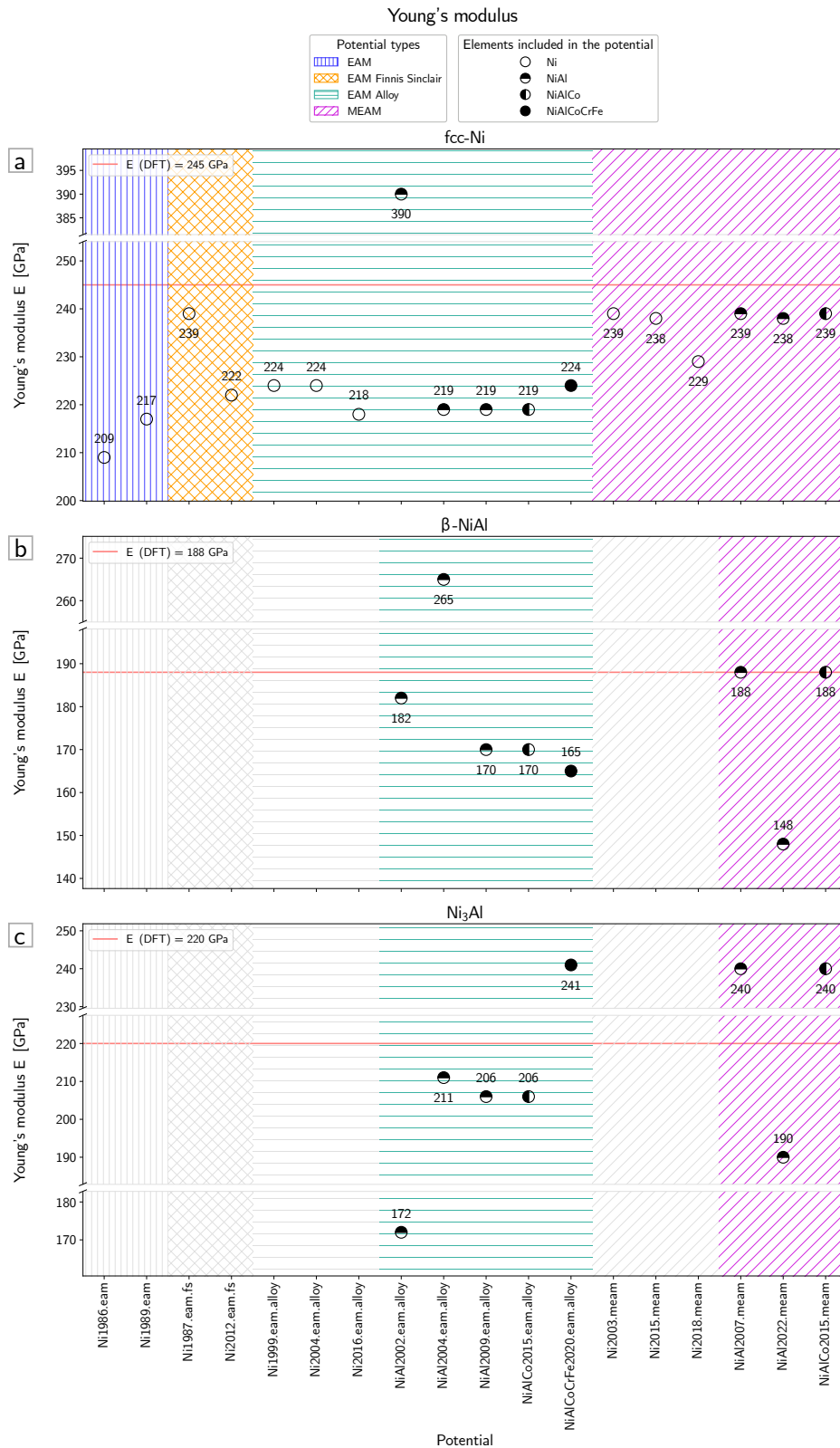
Figure 13: Young's modulus E for a) the pure nickel phase (fcc Ni) of each potential, and b) the β-NiAl and c) the Ni$_3$Al phase of all potentials developed for alloy systems. The red line marks the reference value from DFT. The y-axes are broken to cover the range of all calculated values.

4.2.5 Poisson's ratio

The last elastic property that was calculated from the elastic constants is the Poisson's ratio. It was not used in the potentials' fitting procedures, and Equation (19) was applied to the experimental values mentioned in the respective papers, yielding a result for each potential that will be referred to as "input value".

The first-principles reference for the Poisson's ratio of pure nickel is 0.29 [47, 48, 51]. The calculated values from the potentials are shown in Figure 14a. The overall agreement with the *ab initio* value is good. Ni1986.eam results in a value that is furthest off of the DFT value (6 % higher) except for NiAl2002.eam.alloy which exceeds it by 19 %. Ni1989.eam predicts a result that is just 3 % higher than the DFT value. The two EAM/FS potentials match the first-principles reference almost exactly. All EAM/Alloy potentials except NiAl2002.eam.alloy yield results deviating less than 3 % from the *ab initio* reference. Apart from Ni2018.meam, the MEAM potentials lead to very good results that match the DFT value with a deviation from less than 1 %. Ni2018.meam overestimates the DFT reference by 3 %.

Figure 14b shows the results for the β-NiAl phase for the Poisson's ratio, comparing it to the DFT value of 0.31 [47, 49, 51]. As expected, NiAl2002.eam.alloy predicts this value exactly, having been optimized for this phase. Interestingly, NiAl2009.eam.alloy and NiAlCo2015.eam.alloy result in values that are 4 % higher than the DFT value, while the one obtained with NiAl2004.eam.alloy overestimates it by just 1 %, although the former two were also fitted to properties of the β-NiAl phase. The result for NiAl-CoCrFe2020.eam.alloy falls short of the DFT value by 4 %, possibly because it was fitted to match high entropy alloy (HEA) properties instead of properties of binary phases. All three MEAM potentials deviate from the DFT value. This time however, NiAl2022.eam.alloy is the one closest to the DFT value, resulting in a value that is just 1 % lower than the reference, while the other two are 3 % lower.

In Figure 14c, the Poisson's ratio of Ni_3Al are shown. None of the potentials yield a result matching the *ab initio* value of 0.29 [47, 50, 51]. NiAl2002.eam.alloy is very far off again, predicting a result 32.5 % higher than the reference. However, neither NiAl2004.eam.alloy nor NiAl2009.eam.alloy or NiAlCo2015.eam.alloy match the DFT reference, the first overestimating it by 6 %, the latter two by 10 %. NiAlCoCrFe2020.eam.alloy does not yield a reasonable result at all, underestimating the *ab initio* value by 56 %. Contrary, the MEAM potentials result in values closest to the DFT reference, but not matching it exactly either.
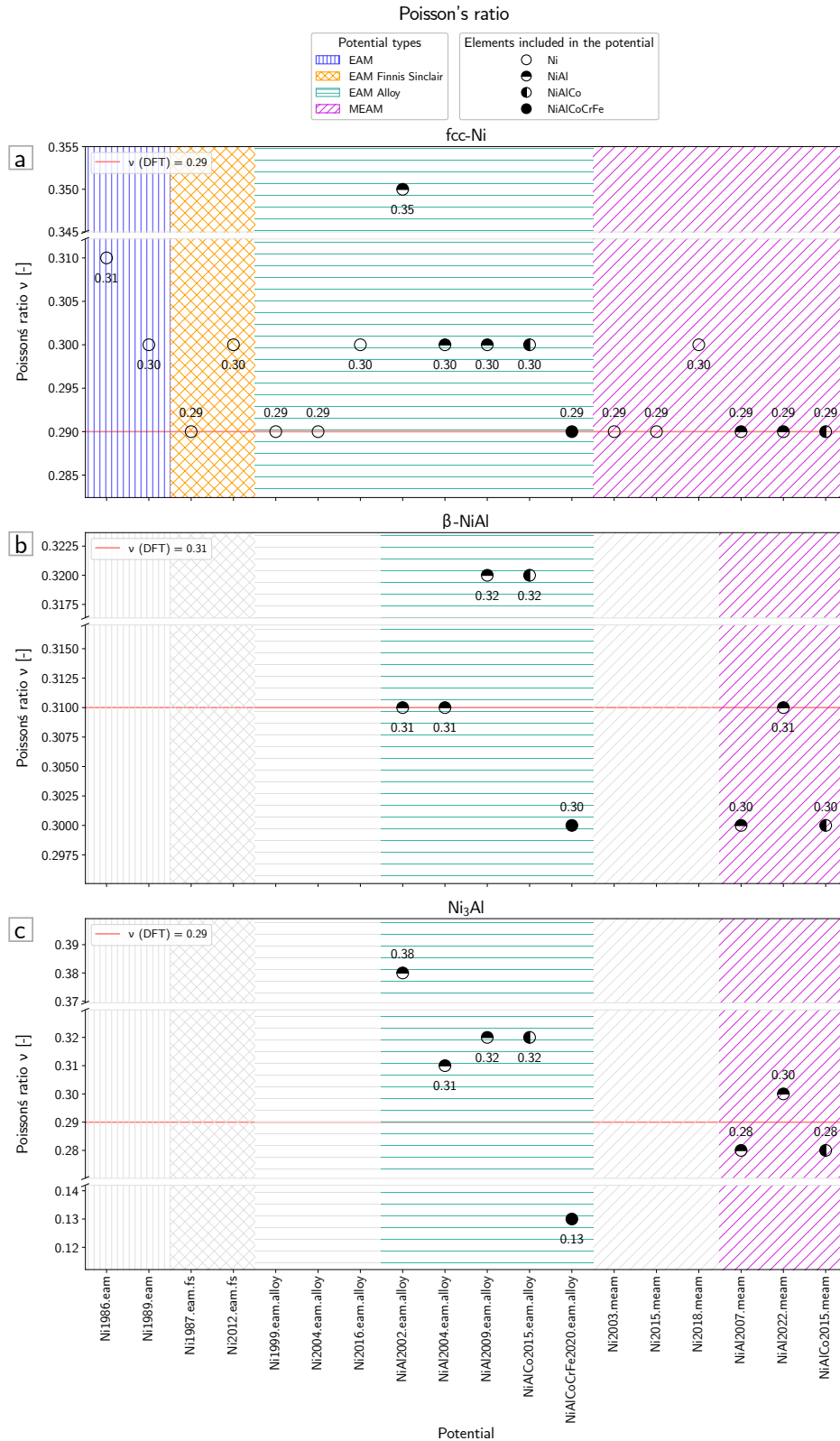
Figure 14: Poisson's ratio ν for the a) pure nickel phase (fcc Ni) of each potential, and b) the β-NiAl and c) the Ni$_3$Al phase of all potentials developed for alloy systems. The red line marks the reference value from DFT. The y-axes are broken to cover the range of all calculated values.

4.3 Vacancy formation energies

The last property that was evaluated for all three phases is the vacancy formation energy. This property was used in the fitting process of most of the potentials, and should therefore agree well with the experimental values. In Figure 15, the effective point defect energies of a nickel monovacancy are compared: the results for pure nickel (fcc) in Figure 15a, for β-NiAl in Figure 15b and for Ni_3Al in Figure 15c. The *ab initio* reference values are 1.42 eV/atom [52], 0.74 eV/atom [53], and 1.5 eV/atom [54], respectively.

The reference value for pure nickel was calculated using pseudopotentials using the projector augmented wave (PAW) formalism, and applying the Perdew-Burke-Ernzerhof (PBE) version of the generalized gradient approximation (GGA) for the exchange and correlation functionals [46, 55]. Those parameters were used for all other properties that have been calculated in this thesis. For the other two phases, we did not find results calculated with the parameters that were just mentioned, therefore the reference values for the other two phases are based on different concepts. The reference values obtained with these parameters were chosen because of their availability, and it is just as valid to compare to values calculated using any other parameters. The *ab initio* value for the β-NiAl phase was obtained with a mixed-basis approach pseudopotential and the local density approximation (LDA) as proposed by Kohn and Sham in [2] for the exchange and correlation energies. For the Ni_3Al phase, the DFT value was obtained using ultrasoft pseudopotentials and the GGA as per Perdew and Wang (PW86) for the exchange functionals[56]. It was calculated for a temperature of 1400 K, but according to the authors, the influence of temperature is very small [54]. They provided another value of 1.95 eV/atom, using the LDA as proposed by Ceperley and Alder and with the parametrization proposed by Perdew and Zunger [57, 58], which allows to see the tendency of LDA to overestimate binding energies, while using GGA tends to lead to underestimate them.

Figure 15a shows the nickel vacancy formation energy in pure nickel which are compared to the DFT reference of 1.42 eV/atom [52]. Ni1986.eam and Ni1989.eam overestimate the vacancy formation energy by 15 and 20 %, respectively, but match their experimental input very well. Ni1987.eam.fs matches the DFT reference, as the experimental value used for fitting was 1.4-1.46 eV/atom [20]. The second EAM/FS potential overestimates this property distinctly, by 24 %. Ni1999.eam.alloy and NiAlCoCrFe2020.eam.alloy match the experimental input and are therefore 13 % higher than the *ab initio* reference. Ni2004.eam.alloy overestimates it by 19 %, while NiAl2002.eam.alloy underestimates it by 60 %. All other EAM/Alloy potentials yield the same result, exceeding the first-principles reference by 11 %. Ni2003.meam, NiAl2007.meam and NiAl2015.meam result in lower values than the experimental fitting value, but therefore overestimate the DFT value by

just 6 %. Ni2015.meam and NiAl2022.meam result in low values and are not suitable to calculate the vacancy formation energy. Ni2018.meam gives a result which is relatively close to the DFT value, but also significantly lower than the experimental fitting value.

The formation energies of a nickel monovacancy in the β-NiAl phase are shown in Figure 15b and will be compared to an *ab initio* reference of 0.74 eV/atom. Regardless of the parametrization for the DFT calculation and trends arising from it, the MD results for this property vary strongly. They do not seem to be following trends similar to those observed for other properties either. NiAl2002.eam.alloy underestimates the first-principles reference by 39 %, while NiAl2004.eam.alloy exceeds it by 34 %. NiAl2009.eam.alloy and NiAlCo2015.eam.alloy yield the same result which is 19.5 % higher than the DFT reference. The HEA potential NiAlCoCrFe2020.eam.alloy underestimates the DFT value by 27 %. While the result obtained with NiAl2022.meam exceeds the DFT value by 82 %, the other two MEAM potentials match the first-principles reference very well.

In Figure 15c, the nickel vacancy formation energies in Ni$_3$Al are shown. They are compared to the DFT reference of 1.5 eV/atom which was obtained using the GGA. Once again, NiAl2002.eam.alloy is not able to yield reasonable results for this phase, underestimating the value by 50 %. The three EAM/Alloy potentials optimized for Ni$_3$Al (among other phases) predict this property well, each of them overestimating it by less than 8 %. NiAlCoCrFe2020.eam.alloy falls short of it by 26 %. NiAl2007.meam and NiAlCo2015.meam yield a result 6 % lower than the DFT reference, while NiAl2022.meam underestimates it by 59 %. Since none of the potentials overestimate the GGA value by more than 8 %, they all strongly underestimate the LDA value of 1.95 eV/atom [54]. The tendency of overestimating binding energies when using LDA is prominent.
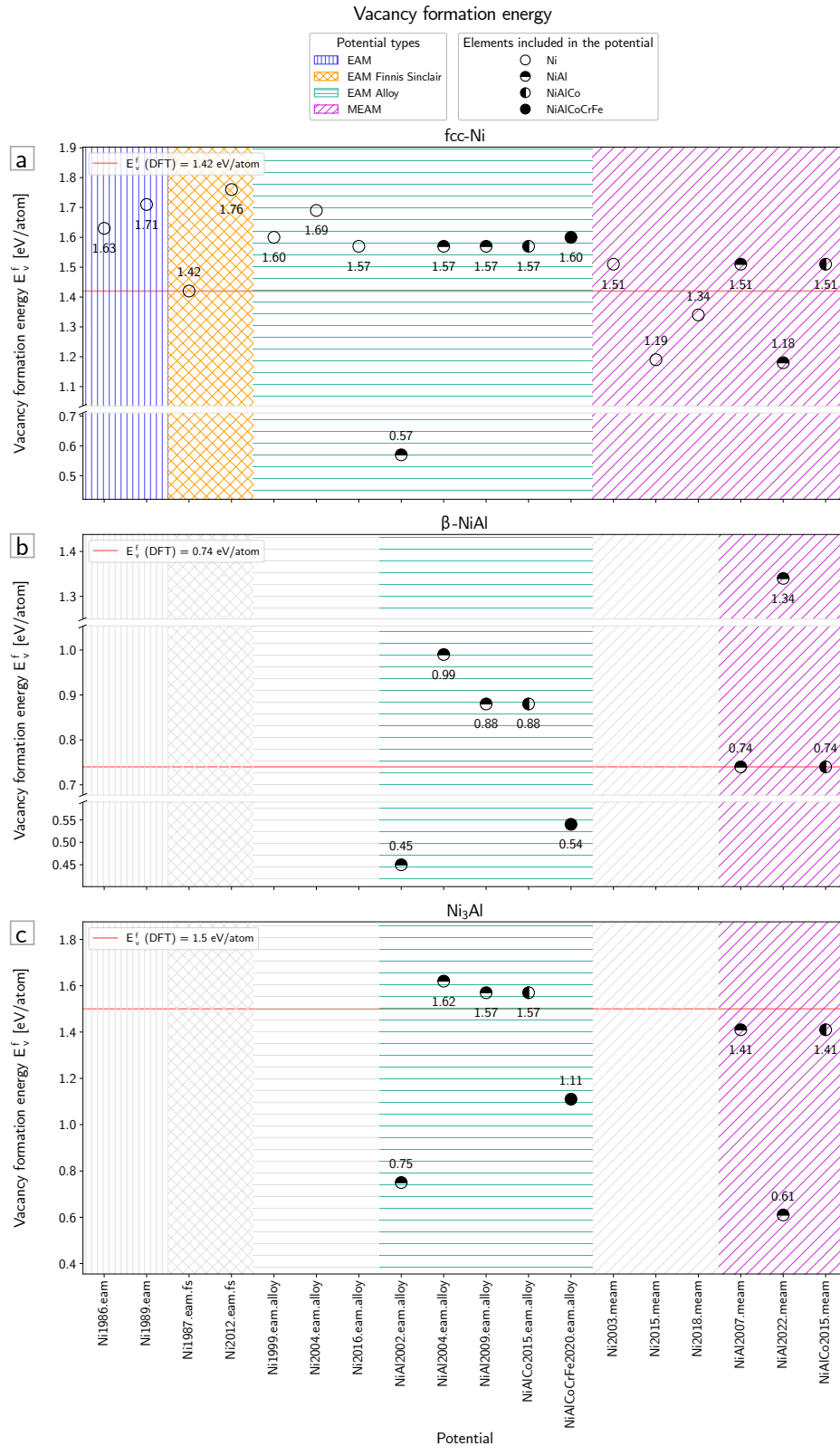
Figure 15: Effective nickel vacancy formation energies E_v^f for a) the pure nickel phase (fcc Ni) of each potential, and b) the β-NiAl and c) the Ni$_3$Al phase of all potentials developed for alloy systems. The red line marks the reference value from DFT. The y-axes are broken to cover the range of all calculated values.

4.4 Stacking fault energies

The last three properties are evaluated for pure fcc nickel only. The energies of extrinsic and intrinsic stacking faults are shown in Figure 16a and b. The DFT value of 129 mJ/m² for the intrinsic and 126 mJ/m² for the extrinsic stacking faults from [59] and the average experimental value of 125 mJ/m² that can be found in most papers are very close together. Some of the potentials included the intrinsic stacking fault in their fitting database and should therefore reproduce the experimental value fairly well. While we could not found extrinsic stacking fault energies calculated with first-principles methods, both extrinsic and intrinsic stacking fault energies should be very similar. The calculated values follow the exact same trends, just the absolute values deviate very slightly.

None of the EAM potentials were fitted to any planar properties and therefore strongly underestimate the stacking fault energies by nearly 90 %. Ni1987.eam.fs predicts a marginally higher result, but the value is still very far off the DFT reference. Ni2012.eam.fs follows an opposing trend and yields a very high result, exceeding it by more than 50 %. Neither of the EAM/FS potentials included stacking fault energies in their fitting database. Ni1999.eam.alloy and NiAlCoCrFe2020.eam.alloy almost exactly reproduce the experimental input value used in the potential development and are therefore very close to the *ab initio* reference, matching it almost exactly. Ni2004.eam.alloy yields a low result, falling short of the DFT value by about 20 %. Ni2016.eam.alloy, NiAl2004.eam.alloy, NiAl2009.eam.alloy and NiAlCo2015.eam.alloy all yield the same result, which is 6 % higher than the first-principles value. These four potentials did not include the stacking fault energies as a fitting parameter. Once again, NiAl2002.eam.alloy does not lead to a good result, overestimating the property by roughly 200 %. Ni2003.meam, NiAl2007.meam and NiAlCo2015.meam were fitted to the stacking fault energy, match the experimental input value and the DFT value very well. This is not the case for Ni2015.meam, Ni2018.meam and NiAl2022.meam, none of which have been fitted to stacking fault energies. Ni2018.meam underestimates it by 57 %, the other two MEAM potentials are just marginally better, falling short of the DFT value by 48 %.
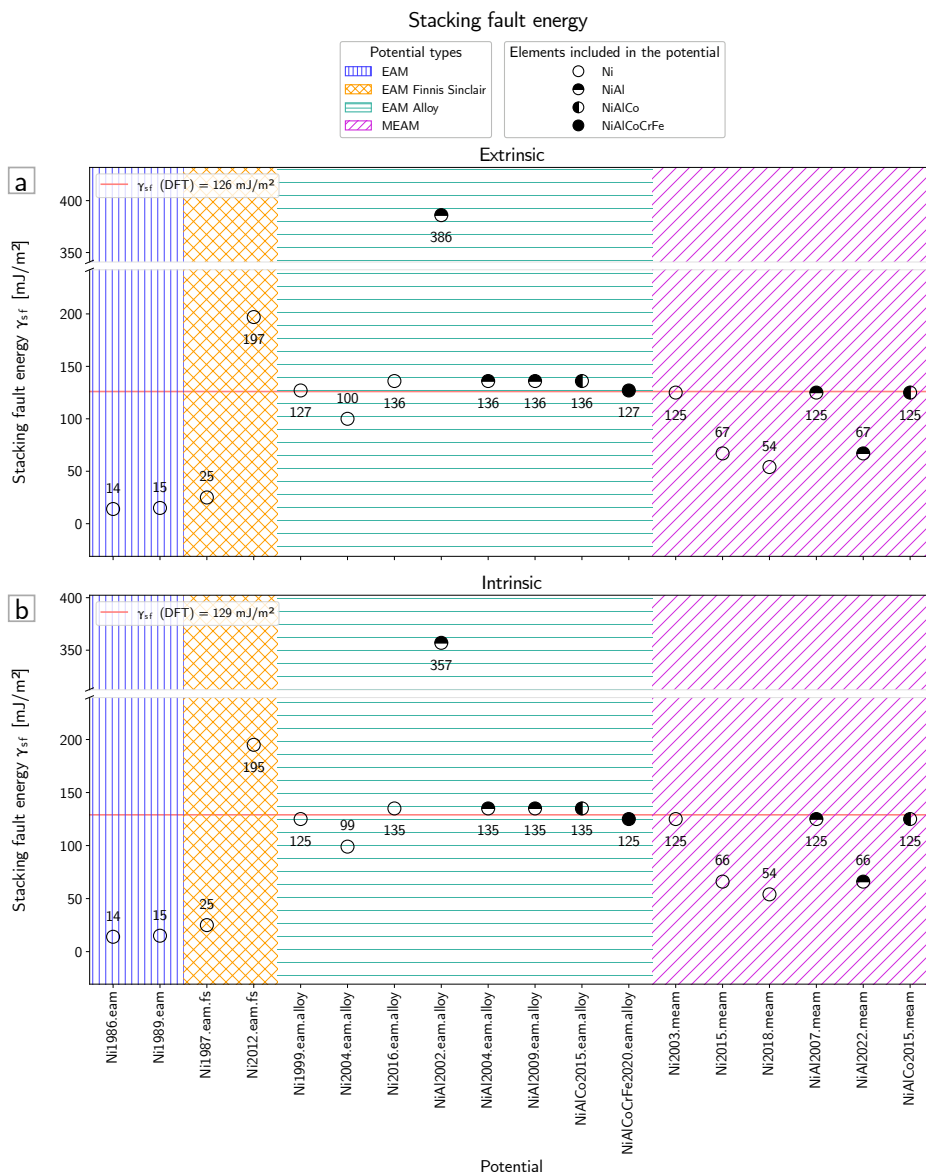
Figure 16: Stacking fault energies γ_{sf} for a) extrinsic and b) intrinsic stacking faults for the pure nickel phase (fcc Ni) of each potential. The red line marks the reference value from DFT. The y-axes are broken to cover the range of all calculated values.

4.5   Surface energies

The results for the surface energies for the (100), (110) and (111) surfaces of the pure nickel phase have been calculated for all potentials and are shown in Figure 17a, b and c, respectively.

Even if surface energies were included in the fitting database of a potential, the calculated values are still significantly lower than the experimental target values, and also lower than the DFT values. The DFT references are 2208 mJ/m^2, 2286 mJ/m^2 and 1924 mJ/m^2 for the (100), (110) and (111) surfaces, respectively [47, 48]. However, they still are in the correct order of magnitude and do follow the trend that can be observed in results obtained with DFT methods: the surface energy for the (110) surface is higher than the (100) surface energy, which itself is higher than the energy for the (111) surface.

Both EAM and both EAM/FS potentials yield significantly lower results for all three surface energies than the experimental and DFT values, underestimating them by 22 to 36 %. However, they followed the trend that was just mentioned. None of those potentials were fitted to any planar defect properties. Except for Ni1999.eam.alloy (and therefore NiAlCoCrFe2020.eam.alloy), which were fitted to match the trend known from DFT and a general reference value of 2280 mJ/m^2, none of the EAM/Alloy potentials were fitted to any planar defect input values either. Those two potentials underestimate the surface energies by 10 to 15 %, while all other EAM/Alloy potentials except NiAl2002.eam.alloy are 7 to 15 % lower than the first-principles reference. NiAl2002.eam.alloy falls short of the DFT value by 35 to 44 %, but the trend can be observed for this potential, too. Ni2003.meam, NiAl2007.meam and NiAlCo2015.meam yield good results that all deviate by less than 17 %; however, they are expected to predict reasonable results because they were fitted to experimental surface energies. While Ni2015.meam and Ni2018.meam included those properties in the fitting process too, they yield lower results for all three surfaces, all lower than 18 % of the DFT reference. NiAl2022.meam results in similar values.

The trend observed in DFT calculations is present for all tested interatomic potentials, too. Most potentials also seem to follow another trend, yielding minimum relative errors to the DFT value for the (111) surface energy, while the relative errors of the (100) and (110) surface energies are mostly quite similar.
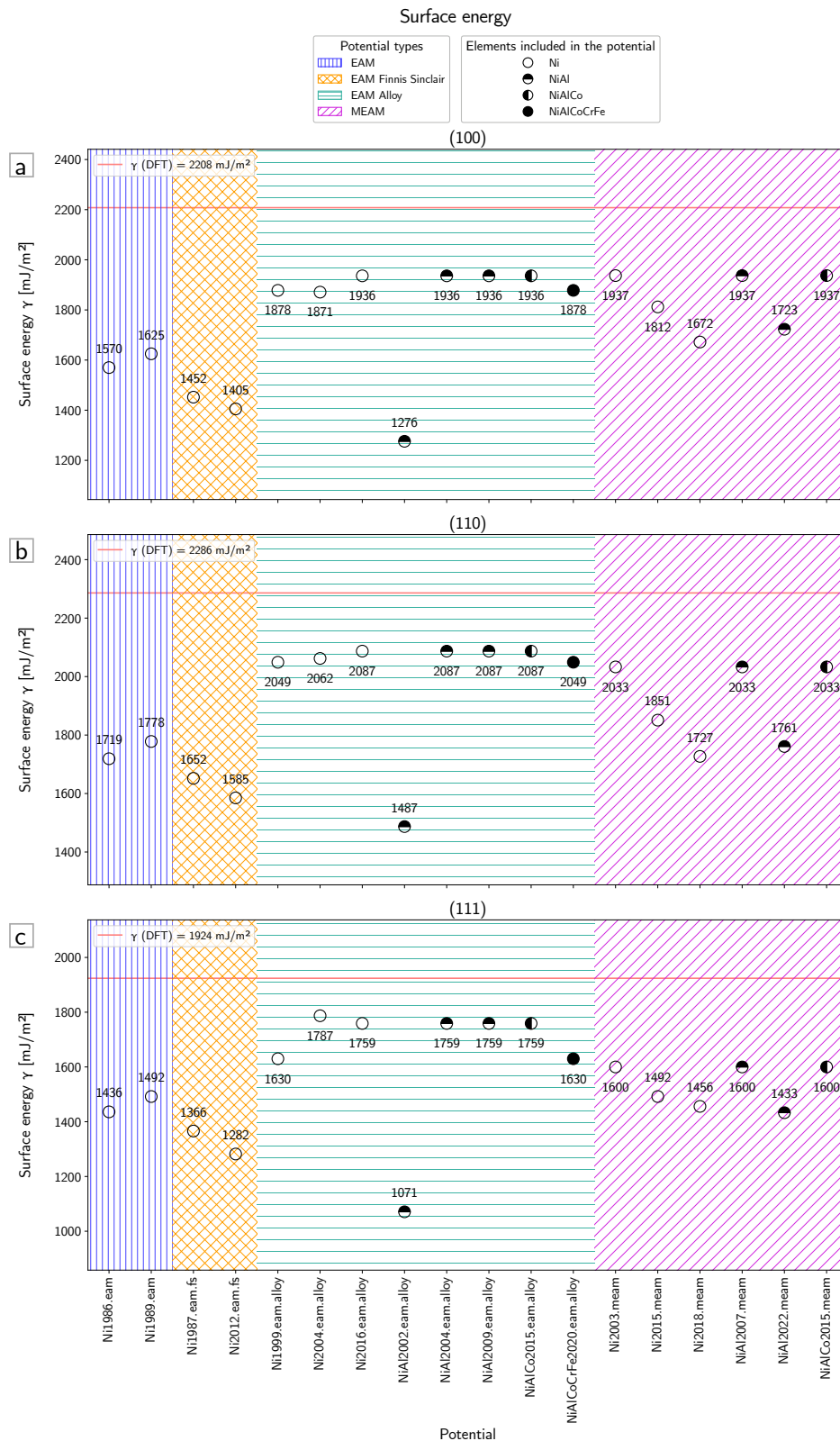
Figure 17: Surface energies γ for the a) (100), b) (110) and c) (111) surfaces for the pure nickel phase (fcc Ni) of each potential. The red line marks the reference value from DFT.

4.6   Grain boundary energy

Figure 18 shows the results for the last property, the grain boundary energy of a symmetric tilt Σ_5 grain boundary. The *ab initio* reference is 1383 mJ/m$^\mathbf{2}$ [47, 48].

None of the potentials included this property in their fitting procedure, and there is only one paper providing a reference value. However, Ni1986.eam predicts a nearly perfect fit to the DFT value, and Ni1989.eam as well as Ni1987.eam.fs are close to the reference, too. Ni2012.eam.fs results in the highest value, significantly exceeding the DFT value by 19 %. None of the EAM and EAM/FS potentials included any planar properties in their potential development. The grain boundary energy for Ni1999.eam.alloy reported in [22] is 1572 mJ/m$^\mathbf{2}$, which was met by the result in this thesis, but is 13 % higher than the DFT value. No planar properties were used for fitting this potential. Although there is no reference value in the respective paper, NiAlCoCrFe2020.eam.alloy, being based on Ni1999.eam.alloy, yields the same result. Ni2004.eam.alloy yields a result 8 % lower than the DFT value. Ni2016.eam.alloy, NiAl2004.eam.alloy, NiAl2009.eam.alloy and NiAlCo2015.eam.alloy all result in a value very close to the *ab initio* reference, underestimating it by just 2 %. No planar properties were used for developing these potentials. NiAl2002.eam.alloy leads to a very low result, underestimating the first-principles value by 30 %. Ni2003.meam, NiAl2007.meam and NiAlCo2015.meam match the DFT value very well, most likely because they were fitted to experimental stacking fault and surface energies. Ni2015.meam, Ni2018.meam and NiAl2022.meam predict lower values, in agreement with their behaviour for the other planar defect energies.
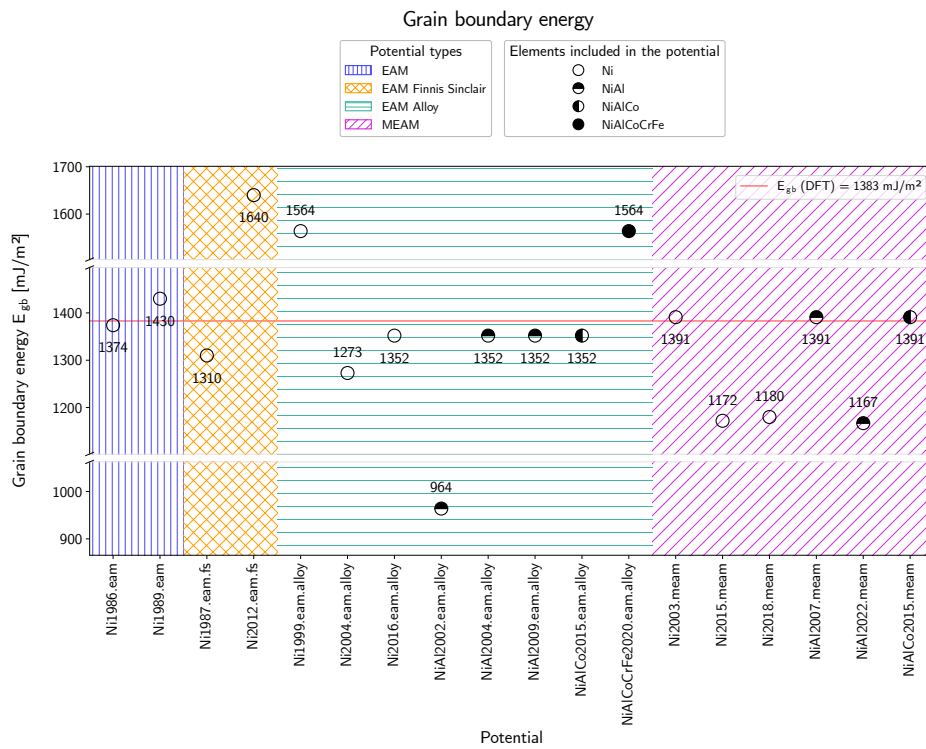
Figure 18: Energy of the Σ_5 grain boundary E_{gb} for the pure nickel phase (fcc Ni) of each potential. The red line marks the reference value from DFT. The y-axis is broken to cover the range of all calculated values.

5   Conclusion

The ability of different interatomic potentials developed for nickel-based material systems to predict different material properties that match results from *ab initio* calculations was evaluated. The properties evaluated in this thesis were chosen to be ones that are frequently calculated with DFT methods, too.

The accuracy of the predictions of pure fcc nickel properties varies strongly with the calculated property, the potential type as well as the input values used for potential development. A majority of the calculated results underestimated the DFT values. Generally, properties included in the fitting processes were close to the DFT values, especially if the experimental values used for fitting were close to the *ab initio* reference. This is particularly true for the elastic properties, while the equilibrium lattice parameter matched the experimental instead of the *ab initio* value. Vacancy formation energies tend to be overestimated, as they were often fitted to an experimental value, which is generally higher than the DFT value. Both EAM and both EAM/FS potentials were not able to predict DFT stacking fault energies, while EAM/Alloy potentials except for Ni2004.eam.alloy and NiAl2002.eam.alloy yielded good results, even if they were not fitted to experimental values. Ni2004.eam.alloy was developed to predict properties of multilayer systems, while NiAl2002.eam.alloy was optimized for the β-NiAl phase. The MEAM potentials which included stacking fault energies in their fitting process (Ni2003.meam, NiAl2007.meam and NiAlCo2015.meam) matched the DFT values well, while the other MEAM potentials underestimated them significantly. Very accurate results were achieved with the calculation of the Σ_5 grain boundary energies, which agreed exceptionally well with the DFT reference, even if no planar properties were included in the fitting process.

The Ni–Al interactions of all alloy potentials were used to calculate properties of the β-NiAl and the Ni_3Al phases. No planar properties were calculated for these two phases. Depending on which phase or phases a potential was optimized for, the results for properties of those two phases agreed better or worse with first-principle values. The type of potential does not seem to have a strong influence on the results. While the Ni–Al interactions of NiAl2002.eam.alloy were developed to predict β-NiAl properties, NiAl2004.eam.alloy included pure nickel and Ni_3Al properties in its fitting database. NiAl2009.eam.alloy and NiAlCo2015.eam.alloy were optimized for both phases, while NiAlCoCrFe2020.eam.alloy was fitted to equiatomic mixture properties. Properties of both phases were included in the potential fitting process of all three MEAM alloy potentials. Lattice and elastic properties of β-NiAl were met well by all potentials optimized for this phase except NiAl2022.meam, which shows a strong deviation for each result. NiAl2004.eam.alloy and NiAlCoCrFe2020.eam.alloy cannot accurately predict properties for this phase, not

being optimized for it. Vacancy formation energies were mostly strongly over- or under-estimated, but were compared to DFT values obtained with LDA which have a tendency of overestimating binding energies. Vice versa, both lattice and elastic properties matched the DFT values well for potentials fitted to the Ni_3Al phase. Therefore, NiAl2002.eam.alloy is not able to predict results matching the first-principles references, as is NiAlCoCrFe2020.eam.alloy. The other three EAM/Alloy potentials, as well as NiAl2007.meam and NiAlCo2015.meam, show good agreement with the DFT values. Again, NiAl2022.meam does not yield results matching the DFT values. For this phase, the reference values for the vacancy formation energies were obtained with GGA, and close results were obtained with the respectively optimized potentials.

All in all, the best results, i.e. those showing minimum deviation from the DFT references for all three phases, are obtained with NiAl2009.eam.alloy and NiAlCo2015.eam.alloy, as well as NiAl2007.meam and NiAlCo2015.meam which are built on top of Ni2003.meam. Contrary to the MEAM potentials, the EAM/Alloy potentials did not include any planar properties in their fitting procedure, but still were able to yield good results for these properties. The ability of these "simple" interatomic potentials to imitate results obtained with DFT method could be further verified by calculating other planar properties such as energies for different grain boundaries, twin or anti-phase boundaries or developing EAM-type potentials using *ab initio* data as fitting database.

References

[1] M. S. Daw, "Model of metallic cohesion: the embedded-atom method", Physical Review B **39**, 7441–7452 (1989).

[2] W. Kohn and L. J. Sham, "Self-Consistent Equations Including Exchange and Correlation Effects", Phys. Rev. **140**, A1133–A1138 (1965).

[3] R. LeSar, *Introduction to Computational Materials Science: Fundamentals to Applications* (Cambridge University Press, 2013).

[4] J. G. Lee, *Computational Materials Science: An Introduction (1st ed.)* (CRC Press, 2011).

[5] A. Smolyanitsky and V. Tewary, "Numerical simulation of nanoscale systems and materials", in *Modeling, characterization, and production of nanomaterials*, edited by V. K. Tewary and Y. Zhang, Woodhead Publishing Series in Electronic and Optical Materials (2015), pp. 87–111.

[6] R. A. Johnson, "Relationship between Two-Body Interatomic Potentials in a Lattice Model and Elastic Constants", Physical Review B **6**, 2094–2100 (1972).

[7] M. S. Daw and M. I. Baskes, "Embedded-atom method: derivation and application to impurities, surfaces, and other defects in metals", Physical Review B **29**, 6443–6453 (1984).

[8] S. M. Foiles, M. I. Baskes, and M. S. Daw, "Embedded-atom-method functions for the fcc metals Cu, Ag, Au, Ni, Pd, Pt, and their alloys", Physical Review B **33**, 7983–7991 (1986).

[9] S. M. Foiles, "Calculation of the surface segregation of Ni-Cu alloys with the use of the embedded-atom method", Physical Review B **32**, 7685–7693 (1985).

[10] J. H. Rose, J. Ferrante, and J. R. Smith, "Universal Binding Energy Curves for Metals and Bimetallic Interfaces", Physical Review Letters **47**, 675–678 (1981).

[11] Y. Mishin, "Atomistic modeling of the γ and γ'–phases of the Ni–Al system", Acta Materialia **52**, 1451–1467 (2004).

[12] M. W. Finnis and J. E. Sinclair, "A simple empirical N-body potential for transition metals", Philosophical Magazine A **50**, 45–55 (1984).

[13] M. I. Baskes, J. S. Nelson, and A. F. Wright, "Semiempirical modified embedded-atom potentials for silicon and germanium", Physical Review B **40**, 6085–6100 (1989).

[14] M. I. Baskes, "Modified embedded-atom potentials for cubic materials and impurities", Physical Review B **46**, 2727–2742 (1992).

[15] A. P. Thompson, H. M. Aktulga, R. Berger, D. S. Bolintineanu, W. M. Brown, P. S. Crozier, P. J. in 't Veld, A. Kohlmeyer, S. G. Moore, T. D. Nguyen, R. Shan, M. J. Stevens, J. Tranchida, C. Trott, and S. J. Plimpton, "LAMMPS - a flexible simulation

tool for particle-based materials modeling at the atomic, meso, and continuum scales", Computer Physics Communications **271**, 108171 (2022).

[16]NIST Interatomic Potentials Repository, *https://www.ctcms.nist.gov/potentials*, accessed in January 2022, 2010.

[17]C. A. Becker, F. Tavazza, Z. T. Trautt, and R. A. Buarque de Macedoc, "Considerations for choosing and using force fields and interatomic potentials in materials science and engineering", Current Opinion in Solid State and Materials Science **17**, 277–283 (2013).

[18]L. M Hale, Z. T. Trautt, and C. A. Becker, "Evaluating variability with atomistic simulations: the effect of potential and calculation methodology on the modeling of lattice and elastic constants", Modelling and Simulation in Materials Science and Engineering **26**, 055003 (2018).

[19]J. B. Adams, S. M. Foiles, and W. G. Wolfer, "Self-diffusion and impurity diffusion of fee metals using the five-frequency model and the Embedded Atom Method", Journal of Materials Research **4**, 102–112 (1989).

[20]G. J. Ackland, G. Tichy, V. Vitek, and M. W. Finnis, "Simple N-body potentials for the noble metals and nickel", Philosophical Magazine A **56**, 735–756 (1987).

[21]M. Mendelev, M. Kramer, S. Hao, K. Ho, and C. Wang, "Development of interatomic potentials appropriate for simulation of liquid and glass properties of $NiZr_2$ alloy", Philosophical Magazine **92**, 4454–4469 (2012).

[22]Y. Mishin, D. Farkas, M. J. Mehl, and D. A. Papaconstantopoulos, "Interatomic potentials for monoatomic metals from experimental data and ab initio calculations", Physical Review B **59**, 3393–3407 (1999).

[23]X. W. Zhou, R. A. Johnson, and H. N. G. Wadley, "Misfit-energy-increasing dislocations in vapor-deposited CoFe/NiFe multilayers", Physical Review B **69**, 144113 (2004).

[24]R. Stoller, A. Tamm, L. Béland, G. Samolyuk, G. Stocks, A. Caro, L. Slipchenko, Y. Osetsky, A. Aabloo, M. Klintenberg, and Y. Wang, "The impact of short-range forces on defect production from high-energy collisions", Journal of Chemical Theory and Computation **12**, 2871–2879 (2016).

[25]Y. Mishin, M. J. Mehl, and D. A. Papaconstantopoulos, "Embedded-atom potential for B2-NiAl", Physical Review B **65**, 224114 (2002).

[26]G. Purja Pun and Y. Mishin, "Development of an interatomic potential for the Ni– Al system", Philosophical Magazine **89**, 3245–3267 (2009).

[27]G. P. Purja Pun, V Yamakov, and Y Mishin, "Interatomic potential for the ternary Ni–Al–Co system and application to atomistic modeling of the $B2–L1_0$ martensitic transformation", Modelling and Simulation in Materials Science and Engineering **23**, 065006 (2015).

[28] D. Farkas and A. Caro, "Model interatomic potentials for Fe–Ni–Cr–Co–Al high-entropy alloys", Journal of Materials Research **35**, 3031–3040 (2020).

[29] B.-J. Lee, J.-H. Shim, and M. I. Baskes, "Semiempirical atomic potentials for the fcc metals Cu, Ag, Au, Ni, Pd, Pt, Al, and Pb based on first and second nearest-neighbor modified embedded atom method", Physical Review B **68**, 144112 (2003).

[30] E. Asadi, M. Asle Zaeem, S. Nouranian, and M. Baskes, "Two-phase solid–liquid coexistence of Ni, Cu, and Al by molecular dynamics simulations using the modified embedded-atom method", Acta Materialia **86**, 169–181 (2015).

[31] A. Etesami and E. Asadi, "Molecular dynamics for near melting temperatures simulations of metals using modified embedded-atom method", Journal of Physics and Chemistry of Solids **112**, 61–72 (2017).

[32] A. Costa e Silva, J. Ågren, M. T. Clavaguera-Mora, D. Djurovic, T. Gomez-Acebo, B.-J. Lee, Z.-K. Liu, P. Miodownik, and H. J. Seifert, "Applications of computational thermodynamics – the extension from phase equilibrium to phase transformations and other properties", Calphad **31**, 53–74 (2007).

[33] A. Mahata, T. Mukhopadhyay, and M. Asle Zaeem, "Modified embedded-atom method interatomic potentials for Al–Cu, Al–Fe and Al–Ni binary alloys: From room temperature to melting point", Computational Materials Science **201**, 110902 (2022).

[34] Y.-K. Kim, W.-S. Jung, and B.-J. Lee, "Modified embedded-atom method interatomic potentials for the Ni–Co binary and the Ni–Al–Co ternary systems", Modelling and Simulation in Materials Science and Engineering **23**, 055004 (2015).

[35] "PyLammps Python wrapper class", accessed in January 2022, `https://git.ecdf.ed.ac.uk/multiscale/lammps/tree/09ca7b32fc3161cc4302a5922835a246d6998530/python/examples/pylammps` (2016).

[36] M. Tschopp, "LAMMPS Tutorial 1", accessed in January 2022, `https://github.com/mrkllntschpp/lammps-tutorials/blob/master/LAMMPS-Tutorials-01.ipynb` (2020).

[37] A. P. Thompson, "ELASTIC", accessed in January 2022, `https://github.com/lammps/lammps/tree/develop/examples/ELASTIC` (2010).

[38] M. Tschopp, "LAMMPS Vacancy Formation Energy", accessed in January 2022, `https://icme.hpc.msstate.edu/mediawiki/index.php/LAMMPS_Vacancy_Formation_Energy.html` (2014).

[39] M. Tschopp, "LAMMPS Intrinsic Stacking-Fault Energy", accessed in January 2022, `https://icme.hpc.msstate.edu/mediawiki/index.php/LAMMPS_Intrinsic_Stacking-Fault_Energy.html` (2014).

[40]M. Tschopp, "LAMMPS Grain Boundary", accessed in January 2022, `https://github.com/mrkllntschpp/lammps-tutorials/blob/master/LAMMPS-Tutorials-05.ipynb` (2020).

[41]M. Sprik, R. W. Impey, and M. L. Klein, "Second-order elastic constants for the Lennard-Jones solid", Physical Review B **29**, 4368–4374 (1984).

[42]W. Voigt, *Lehrbuch der Kristallphysik (mit Ausschluß der Kristalloptik)*, Vol. 34 (BG Teubner, 1910).

[43]A. Reuss, "Berechnung der Fließgrenze von Mischkristallen auf Grund der Plastizitätsbedingung für Einkristalle.", Zeitschrift für Angewandte Mathematik und Mechanik (Journal of Applied Mathematics and Mechanics) **9**, 49–58 (1929).

[44]R. Hill, "The Elastic Behaviour of a Crystalline Aggregate", Proceedings of the Physical Society. Section A **65**, 349–354 (1952).

[45]Y. Mishin and C. Herzig, "Diffusion in the Ti–Al system", Acta Materialia **48**, 589–623 (2000).

[46]J. P. Perdew, K. Burke, and M. Ernzerhof, "Generalized Gradient Approximation Made Simple", Physical Review Letters **77**, 3865–3868 (1996).

[47]A. Jain, S. P. Ong, G. Hautier, W. Chen, W. D. Richards, S. Dacek, S. Cholia, D. Gunter, D. Skinner, G. Ceder, and K. A. Persson, "Commentary: the materials project: a materials genome approach to accelerating materials innovation", APL Materials **1**, 011002 (2013).

[48]The Materials Project, "Materials Data on Ni by Materials Project", accessed in June 2022, `10.17188/1199153` (2020).

[49]The Materials Project, "Materials Data on AlNi by Materials Project", accessed in June 2022, `10.17188/1190944` (2020).

[50]The Materials Project, "Materials Data on AlNi$_3$ by Materials Project", accessed in June 2022, `10.17188/1201079` (2020).

[51]M. de Jong, W. Chen, T. Angsten, A. Jain, R. Notestine, A. Gamst, M. Sluiter, C. K. Ande, S. van der Zwaag, J. J. Plate, C. Toher, S. Curtarolo, G. Ceder, K. A. Persson, and M. Asta, "Charting the complete elastic properties of inorganic crystalline compounds", Scientific Data **2**, 150009 (2015).

[52]P. Nandi, M. Valsakumar, S Chandra, H. Sahu, and C. Sundar, "Efficacy of surface error corrections to density functional theory calculations of vacancy formation energy in transition metals", Journal of Physics: Condensed Matter **22**, 345501 (2010).

[53]B. Meyer and M. Fähnle, "Atomic defects in the ordered compound B2-NiAl: a combination of ab initio electron theory and statistical mechanics", Physical Review B **59**, 6072–6082 (1998).

[54]H. Schweiger, O. Semenova, W. Wolf, W. Püschl, W. Pfeiler, R. Podloucky, and H. Ipser, "Energetics of point defect formation in Ni_3Al", Scripta Materialia **46**, 37–41 (2002).

[55]P. E. Blöchl, "Projector augmented-wave method", Physical Review B **50**, 17953–17979 (1994).

[56]J. P. Perdew and W. Yue, "Accurate and simple density functional for the electronic exchange energy: generalized gradient approximation", Physical Review B **33**, 8800–8802 (1986).

[57]D. M. Ceperley and B. J. Alder, "Ground state of the electron gas by a stochastic method", Physical Review Letters **45**, 566–569 (1980).

[58]J. P. Perdew and A. Zunger, "Self-interaction correction to density-functional approximations for many-electron systems", Physical Review B **23**, 5048–5079 (1981).

[59]M. Chandran and S. K. Sondhi, "First-principle calculation of stacking fault energies in Ni and Ni-Co alloy", Journal of Applied Physics **109**, 103525 (2011).